Comparison of iterative parametric and indirect deep learning-based reconstruction methods in highly undersampled DCE-MR Imaging of the breast

Aditya Rastogi and Phaneendra K. Yalavarthy[a)]
Department of Computational and Data Sciences, Indian Institute of Science, Bangalore 560012, India

(Received 19 April 2020; revised 24 July 2020; accepted for publication 3 August 2020;
published 6 September 2020)

Purpose: To compare the performance of iterative direct and indirect parametric reconstruction methods with indirect deep learning-based reconstruction methods in estimating tracer-kinetic parameters from highly undersampled DCE-MR Imaging breast data and provide a systematic comparison of the same.

Methods: Estimation of tracer-kinetic parameters using indirect methods from undersampled data requires to reconstruct the anatomical images initially by solving an inverse problem. This reconstructed images gets utilized in turn to estimate the tracer-kinetic parameters. In direct estimation, the parameters are estimated without reconstructing the anatomical images. Both problems are ill-posed and are typically solved using prior-based regularization or using deep learning. In this study, for indirect estimation, two deep learning-based reconstruction frameworks namely, ISTA-Net$^+$ and MODL, were utilized. For direct and indirect parametric estimation, sparsity inducing priors ($L1$ and Total-Variation) and limited memory Broyden-Fletcher-Goldfarb-Shanno algorithm as solver was deployed. The performance of these techniques were compared systematically in estimation of vascular permeability (K_{trans}) from undersampled DCE-MRI breast data using Patlak as pharmaco-kinetic model. The experiments involved retrospective undersampling of the data 20×, 50×, and 100× and compared the results using PSNR, nRMSE, SSIM, and Xydeas metrics. The K_{trans} maps estimated from fully sampled data were utilized as ground truth. The developed code was made available as https://github.com/Medical-Imaging-Group/DCE-MRI-Compare open-source for enthusiastic users.

Results: The reconstruction methods performance was evaluated using ten patients breast data (five patients each for training and testing). Consistent with other studies, the results indicate that direct parametric reconstruction methods provide improved performance compared to the indirect parameteric reconstruction methods. The results also indicate that for 20× undersampling, deep learning-based methods performs better or at par with direct estimation in terms of PSNR, SSIM, and nRMSE. However, for higher undersampling rates (50× and 100×) direct estimation performs better in all metrics. For all undersampling rates, direct reconstruction performed better in terms of Xydeas metric, which indicated fidelity in magnitude and orientation of edges.

Conclusion: Deep learning-based indirect techniques perform at par with direct estimation techniques for lower undersampling rates in the breast DCE-MR imaging. At higher undersampling rates, they are not able to provide much needed generalization. Direct estimation techniques are able to provide more accurate results than both deep learning- and parametric-based indirect methods in these high undersampling scenarios. © *2020 American Association of Physicists in Medicine* [https://doi.org/10.1002/mp.14447]

Key words: AIF, breast imaging, DCE-MRI, deep learning, fast imaging, ISTA-Net, perfusion imaging, under-sampling

1. INTRODUCTION

Early detection of pathologies is vital for reducing mortality and morbidity and with the development of various medical imaging techniques, clinicians are able to provide early and accurate diagnosis on the basis of anatomical manifestation of these pathologies. In the past few years, techniques have been developed, which can show both physical and physiological manifestation of the diseases. One such technique is dynamic contrast enhanced (DCE) magnetic resonance imaging (MRI)[1] in which a T_1 shortening contrast agent[2] (CA) gets injected into the bloodstream and T_1 weighted scans of the organ of interest are taken after that. This technique of acquiring three-dimensional (3D) data with time results in Dynamic MR Imaging and based on the collected dynamic data one can measure the physiological characteristics of both healthy and unhealthy tissues. In DCE-MRI, one takes advantage of the fact that the vasculature near the unhealthy tissue will behave differently than that of its counterpart's, for example, the vasculature formed by malignant tumor tissues is leaky and this causes the contrast agent to permeate through the vessels and accumulate in extracellular extravascular space (EES).

In any contrast-based imaging method, traditional expert analysis would involve subjective evaluation of the enhanced voxels in region of interest (ROI). Apart from being observer dependent, this method may not provide quantifiable parameters or measurements. To enable this, many methods for quantitative analysis of DCE-MRI were proposed, that can be divided into two groups namely, nonparametric (model free) and parametric methods. Nonparametric methods analyze DCE-MRI data by characterizing the shape and size of signal intensity over time at a voxel in ROI. Indices commonly utilized in nonparametric analysis are peak enhancement (ΔS), wash-in,[3] wash-out[4] slope, time to peak enhancement (T_P), signal enhancement ratio (SER),[5] and area under curve (AUC). These indices are intuitive, can be inferred directly through images without finding CA concentrations, computationally cheap and does not require computation of Arterial Input Function (AIF). These indices are correlated with the physiological behavior of tissues for example, increased wash-in can indicated growth in tumor or improvement in organ functionality (in case of renal transplant).

However, these indices are dependent on gray scale values of the image and, therefore, are influenced by scanner settings and type.[6] Moreover, even though these indices are correlated with the physiological behavior of tissue, they may not provide physiological information like vascular permeability and vascular density. These parameters can be estimated using parametric methods of DCE-MRI analysis. In parametric analysis, mathematical pharmaco-kinetic (PK) models gets utilized with input being CA concentration maps. These methods, include earlier investigations by Tofts,[7] Larson,[8] Patlak,[9] and Brix,[10] in study of brain tumors and other diseases. Many PK models exist in the literature for DCE-MR imaging and they were based on different assumptions about tissue physiology to provide computational tractability. However, unlike nonparametric methods, parametric methods require AIF for parameter estimation. Two main categories of PK models are compartmental models and spatially distributed models. In both models, the CA exchange between blood and tissue has been modeled as exchange between multiple interacting compartments. In compartmental models, it was assumed that the compartments are homogeneous that is, the concentration of CA in a compartment at a time is uniform and the rate of change in CA concentration is directly proportional to the concentration. Popular compartmental models used for DCE-MRI are Brix model,[10] Patlak model,[9] and eTofts (e - extended) model,[11] two-compartment exchange model (2CXM).[12] All these models assume exchange between two compartments, namely vascular and extravascular extracellular compartments (EES). However because of the mathematical complexity of 2CXM model and the assumption of AIF as a single exponential function makes them less popular than other Patlak and eTofts models. The eTofts model utilizes three parameters namely vascular permeability (K_{trans}), fractional plasma volume (v_p), and volume fraction of EES (v_e). The Patlak model uses the first two parameters only. Physiologically K_{trans} is the most significant parameter and it jointly models the plasma flow (F_P) and tissue permeability. However, in tissue flow limited case, it models F_P and in permeability limited case, it models tissue permeability.

Contrary to compartmental models, the spatial distribution model does not assume homogeneous CA concentration in compartments, instead it assumes a gradient in CA concentration along the flow direction. Popular Spatial distribution models are distributed parameter (DP)[13] and tissue homogeneity (TH) model.[14] However, the complexity of these methods and high computational requirement makes it impractical to deploy in many clinical scenarios.

For accurate estimation of these quantitative parameters, high spatial and temporal resolution is crucial, however improving one comes at the cost of the other. Compressed sensing (CS)-based schemes in MRI[15] have shown promising results by undersampling the k-t space data below Nyquist sampling threshold — undersampling in spatial domain leads to better temporal resolution — and still reconstructing high-resolution anatomical images. This also helps in reducing motion artifacts by reducing the overall scan time. In the past, Smith et al.,[16] Feng et al.,[17] and Rosenkrantz et al.[18] have shown, via experiments on various animal and human scans, that undersampling rates (**R**) of 4-28.7× can be achieved without compromising the diagnostically relevant information. They also used priors such as Total Variation (TV) or wavelet transform, induced by $L_{1/2}$ or L_1 norms as sparsity constraints. These methods computed the anatomical images first, and from them the TK parameters were estimated, and hence known as indirect method of reconstruction.

Contrary to the indirect methods, Guo et al.[19,20] and Dikaois et al.[21] estimated the TK parameters directly from undersampled k-t space data without going into image domain. Their experiments have shown that direct reconstruction methods, perform better than the indirect methods. In Ref. [21] Bayesian inference on prostate cancer dataset was utilized to achieve an undersampling rate of 4×. More recent works ([19,20]) validated direct estimation methods for higher undersampling rate of 100× and gave the flexibility to incorporate any prior. However, both indirect and direct methods mentioned above are solved iteratively and involve regularization. Hence, these methods are computationally expensive and require manual tuning of regularization parameter.

These limitations can be addressed using deep learning (DL) and recent advances in DL have inspired few neural network-based direct estimation of TK parameters. Bliesener et al.[22] estimated K_{trans} from fully sampled data using DL at each pixel individually using one-dimensional (1D) convolution. However, instead of image as input, they used concentration maps and AIF as input. Cagdas et al.[23,24] have estimated the tracer-kinetic parameters through DL using dilated convolution and fully connected layers, where the time dimension was treated as channels. Limitation of such method is the lack of robustness for data with different number of time volumes and inflexibility in choice of PK models. Moreover, they estimated the parameters without taking AIF into account. Kettelkamp et al.[25] modified the network proposed by Cadgas and incorporated AIF as an input to the network as well. However, the inflexibility of such DL methods can be addressed using DL models that reconstruct the anatomical images from which the TK parameters can be estimated. Recently, many networks for image reconstruction have been developed which are based on unrolling of iterative CS schemes like ISTA-Net^{+} [26] and MODL,[27] however, the performance of indirect estimation of TK parameters using DL is yet to be validated against the iterative schemes of reconstruction.

In this work, a systematic comparison was performed between iterative direct and indirect estimation techniques (utilizing different priors) with indirect estimation of TK parameters using DL techniques that are based on compressive sensing iterative schemes for different undersampling rates (**R**) of 20×, 50× and 100×. The breast DCE-MRI data were utilized in the work presented here, as inhomogeneous[28] nature of breast tissue across subjects will be a challenging task for the neural networks to generalize. The performance of the methods presented in this work was quantitatively evaluated using various figures of merit (e.g., PSNR, SSIM, and Xydeas metric). In short, the novelty of this lies in following points: (a). Evaluation of deep learning-based indirect estimation of K_{trans} for different undersampling rates (this maintains the flexibility in terms of number of time volumes and choice of PK model) (b). Detailed comparison between iterative parametric (direct and indirect) estimation and deep learning-based indirect estimation methods and an analysis of the performance of DL models in generalizing inhomogeneous tissues. (c). Providing the assessment of generalizability of deep learning-based inverse methods for the case of DCE-MR imaging of breast.

The rest of this manuscript has been organized as follows: In Section 2, the description of TK parameter estimation pipeline and formulation of the reconstruction problem are presented. In Section 3, the algorithms utilized in this work including the proposed ones are described. In Section 4, the DCE-MRI breast dataset is described along with the experimental procedure and comparison metrics. In Sections 5 and 6, the corresponding results and inferences are presented. These sections also clearly describe the merits as well as the limitation of the proposed approach, and finally the conclusion are presented in Section 7.

2. BACKGROUND

2.A. Notations

The small boldface alphabets such as $\mathbf{x}$ for vectors and capital boldface alphabets like $\mathbf{A}$ for matrices were used throughout this manuscript. The $\mathbf{r}$ describes the spatial location in $3D$ volume in image, that is, $\mathbf{r} \in \{x, y, z\}$ and $\hat{\mathbf{r}}$ was used to denote location in $3D$ volume of frequency domain, that is, $\hat{\mathbf{r}} \in \{k_x, k_y, k_z\}$. The p^{th}-*norm* of any vector $\mathbf{x}$ was denoted as $\|\mathbf{x}\|_p$ and it is defined as $\|x\|_p = (\Sigma_n |x_n|^p)^{1/p}$ where x_n is the n^{th} element of vector $\mathbf{x}$. The small boldface $\mathbf{k}(\hat{\mathbf{r}}, t)$ was utilized to denote fully sampled k-t space data and small boldface $\hat{\mathbf{k}}(\hat{\mathbf{r}}, t)$ to denote undersampled k-t space data. For denoting concentration maps, $CA(\mathbf{r}, t)$ was utilized and for dynamic anatomical images, $s(\mathbf{r}, t)$ was used. Superscript $\mathbf{H}$ was used to denote conjugate transpose of a matrix, if the matrix is real, it is equivalent to transpose of the matrix. Also we use "*" to define Hadamard product between two matrices (element wise multiplication).

2.B. TK parameter modeling

In Tracer Kinetic parameter estimation, one assumes that each voxel to be a tissue consisting of Intra-cellular space, vascular space, and Extra-cellular Extra-vascular space (EES). K_{trans} (min^{-1}) is defined as the rate at which the contrast agent gets accumulated in the EES due to capillary wall permeability. The relation between the Tracer Kinetic (TK) parameters and the undersampled k-t space data has been known as forward modeling and the flow-chart for the same is shown in Fig. 1. For any two-dimensional (2D) slice across axial, coronal, or saggital plane, the matrix in which each entry is the value of a TK parameter at the corresponding location in the image, is known as a map of that particular parameter. The estimation of TK parameter maps from undersampled k-t space data are known as Inverse modeling (Fig. 1). The steps involved in forward modeling are described below:

1. To compute $CA(\mathbf{r},t)$ from TK parameter maps, PK models should be utilized. For the work presented here, Patlak model[9] for determining the TK parameters with population-specific AIF was utilized. For selecting between Patlak model and eTofts model, we calculated the error between concentration value calculated from fully sampled anatomical images $\tilde{CA}(\mathbf{r}, t)$ and concentration values calculated from $K_{trans}(\mathbf{r})$ and $v_p(\mathbf{r})$ that is, $CA(\mathbf{r}, t)$ maps using Eq. (1).

$$\frac{\|CA(\mathbf{r}, t) - \tilde{CA}(\mathbf{r}, t)\|}{\|\tilde{CA}(\mathbf{r}, t)\|} \tag{1}$$

The error in Patlak model was found to be less than eTofts model and hence Patlak model was utilized for all experiments performed in this work. The Patlak model is given by Eq. (2):-

$$CA(\mathbf{r}, t) = v_p(\mathbf{r}) C_p(t) + K_{trans}(\mathbf{r}) \int_0^t C_p(\tau) d\tau \tag{2}$$

where $C_p(t)$ is the AIF defined as the concentration of contrast agent in blood. This equation can be discretized and easily inverted as shown in Eq. (3).

$$CA(\mathbf{r}, t) = v_p(\mathbf{r}) C_p(t) + K_{trans}(\mathbf{r}) \Sigma_{n=0}^{t/\Delta t} C_p(n\Delta t) \Delta t \tag{3}$$

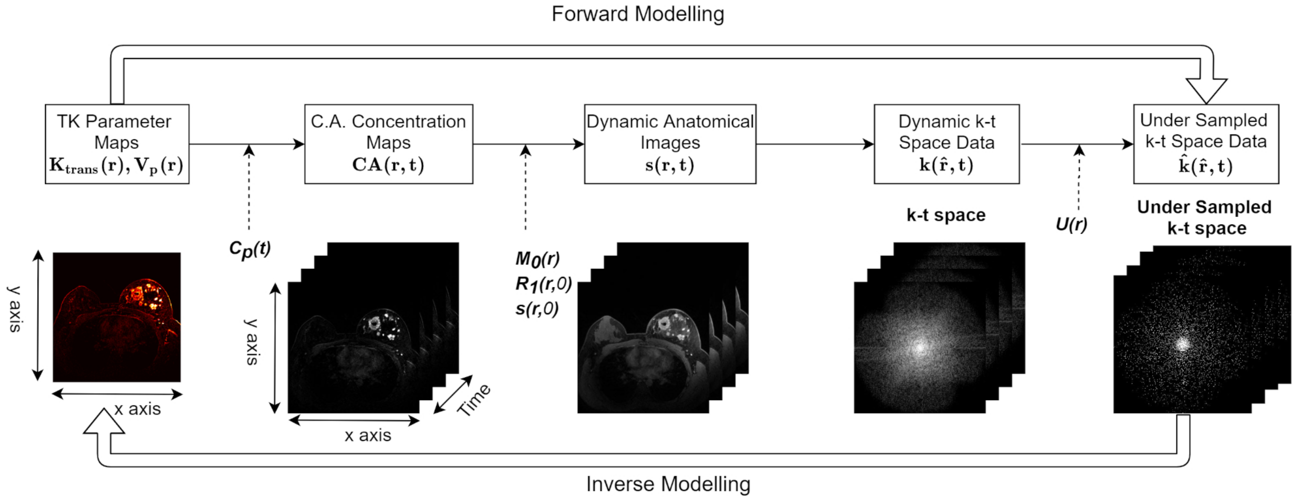

FIG. 1. Flow diagram of forward and inverse modeling of Tracer-kinetic parameters. Patlak[9] model was utilized in computation of the concentration maps and Eq. (4) was deployed to construct dynamic anatomical images from them. Randomized golden-angle radial scheme[17] was used for obtaining undersampled k-t space data. The forward model details were presented in Section 2.B. Black solid arrows represent the steps in forward modeling. Red dashed arrows represent the parameters required for reconstruction. [Color figure can be viewed at wileyonlinelibrary.com]

2. The image signal intensities $s(\mathbf{r}, t)$ can be calculated from the $CA(\mathbf{r}, t)$ values as shown by Eq. (4)

$$s(\mathbf{r},t) = \frac{M_0(\mathbf{r})\sin\alpha(1-e^{-TR\cdot[R_1(\mathbf{r},0)+CA(\mathbf{r},t)\cdot r_1]})}{1-\cos\alpha(e^{-TR\cdot[R_1(\mathbf{r},0)+CA(\mathbf{r},t)\cdot r_1]})} + s(\mathbf{r},0) - \frac{M_0(\mathbf{r})\sin\alpha(1-e^{TR\cdot R_1(\mathbf{r},0)})}{1-\cos\alpha e^{TR\cdot R_1(\mathbf{r},0)}} \tag{4}$$

   Here TR is the repetition time, $R_1(\mathbf{r},0)$ & $M_0(\mathbf{r})$ are pre-contrast R_1 (i.e., $1/T_1$) and longitudinal magnetization at equilibrium, respectively, and α is the flip angle. In this work, the value of $R_1(\mathbf{r},0)$ and $M_0(\mathbf{r})$ were assumed to be constant. The values of α and TR are obtained from the metadata. $s(\mathbf{r}, 0)$ denoted the pre-contrast signal that is, the first time frame volume and r_1 is the contrast agent relaxivity.
3. Undersampled k-t data $\hat{\mathbf{k}}(\hat{\mathbf{r}},t)$ can be obtained from fully sampled $\mathbf{k}(\hat{\mathbf{r}},t)$ by Eq. (5)

$$\hat{\mathbf{k}}(\hat{\mathbf{r}},t) = U(\hat{\mathbf{r}},t) * F(s(\mathbf{r},t)) \tag{5}$$

   where $F(\cdot)$ represents two-dimensional ($2D$) Fourier transform and U is the under-sampling mask generated using randomized golden angle sampling method as mentioned in Ref. [17].

There are different methods to reconstruct K_{trans} maps from undersampled $\hat{\mathbf{k}}(\hat{\mathbf{r}},t)$ data and can be classified broadly into direct and indirect methods of reconstruction. In indirect method of reconstruction,[17,18] anatomical images are first reconstructed from undersampled k-t space data and TK parameters are reconstructed from these images as shown in Eq. (6).

$$s(\mathbf{r},t) = \underset{s(\mathbf{r},t)}{\operatorname{argmin}} \|U(\hat{\mathbf{r}},t) * F(s(\mathbf{r},t)) - \hat{\mathbf{k}}(\hat{\mathbf{r}},t)\|_2^2 + \lambda\|\Gamma s(\mathbf{r},t)\|_p \tag{6}$$

Γ is the domain transform function in which the signal was assumed to be sparse. This optimization problem can be solved with proximal gradient methods[29] like Iterative Shrinkage-Thresholding Algorithm (ISTA) or using augmented Lagrangian methods like alternating direction method of multipliers (ADMM)[30] or plug and play models.[31] Recently, it has been shown that learning the function Γ via deep learning for the specific class of inputs gives better performance than using TV or wavelets as transform functions.[26,27,32]

Direct method of reconstruction[19] reconstructs the TK maps directly from undersampled k-t space data using CS techniques. Earlier works have shown that direct methods perform better than indirect methods for reconstruction of TK parameter maps from highly undersampled data ($\mathbf{R} \geq 20\times$).[19] Accordingly, the loss function can be written as Eq. (7), which can be solved iteratively.

$$K_{trans}(\mathbf{r}), v_p(\mathbf{r}) = \underset{K_{trans},v_p}{\operatorname{argmin}} \|f(K_{trans}, v_p(\mathbf{r})) - \hat{\mathbf{k}}(\hat{\mathbf{r}},t)\|_2^2 \tag{7}$$

where $f(\cdot,\cdot)$ is a function that maps from TK parameters to undersampled k-t space data.

3. METHODS

While iterative methods exist for directly estimating TK parameters from undersampled data,[19] deep learning methods for directly estimating TK parameters have also been attempted before.[23,24] These approaches though perform at par with model-based iterative parameter estimations, have major limitations because of the fully connected layers and stacking the time dimension data as channels in input. Due to these two factors, the network cannot be deployed to scans with different number of time points and/or image dimensions. To provide more generic framework, in this work, indirect estimation using deep learning in which corrupted/noisy anatomical images are reconstructed from undersampled k-t space data, which in turn gets utilized to compute the TK parameters. To address the issue of large dataset requirement in deep learning-based methods, unrolled iterative implementation of algorithms designed to solve CS problems were used. It was shown in Refs. [26] and [27] that using this approach reduces the number of trainable parameters and requires less data. Another approach to estimate the PK parameters is to "denoise" the TK maps estimated from corrupted anatomical images. Solving this problem using classical methods is not feasible because of loss of structural information and deep learning-based methods requires large data, making it unrealistic to be utilized in real-time. These methods along with their pipeline are summarized in Fig. 2, in this work the discussion is limited to implementing methods that are illustrated as **III** and **IV** with K_{trans} being the TK parameter to be recovered. To compare the performance of indirect deep learning-based methods with indirect parametric reconstruction methods, where $TV + L1$ regularization was utilized to provide anatomical MR images and in turn these provide the estimation of K_{trans} map.

3.A. Direct Parametric Reconstruction using sparse recovery methods

For direct reconstruction, using a model-based sparse recovery scheme, the methodology is same as the one given in Ref. [19]. Experiments were also performed using $\|\cdot\|_{TV}$ and $\|\cdot\|_1$ as regularization terms along with Eq. (7) to induce sparsity, where $\|\cdot\|_{TV}$ is anisotropic TV norm. The sparseness constrain is valid due to low permeability of contrast in the majority of breast tissue. The cost-function thus becomes Eq. (8)

$$\begin{aligned} K_{trans}(\mathbf{r}), v_p(\mathbf{r}) = \underset{K_{trans},v_p}{\operatorname{argmin}} & \|f(K_{trans}, v_p(\mathbf{r})) - \hat{\mathbf{k}}(\hat{\mathbf{r}},t)\|_2^2 \\ & + \lambda_1\|K_{trans}(\mathbf{r})\|_{TV} + \lambda_2\|K_{trans}(\mathbf{r})\|_1 \\ & + \lambda_3\|v_p(\mathbf{r})\|_{TV} + \lambda_4\|v_p(\mathbf{r})\|_1 \end{aligned} \tag{8}$$

This equation is solved by a method similar to[19] alternatively minimizing K_{trans} and v_p as shown in Eqs. (9) and (10)

$$\begin{aligned} K_{trans}(\mathbf{r}) = \underset{K_{trans}}{\operatorname{argmin}} & \|f(K_{trans}) - \hat{\mathbf{k}}(\hat{\mathbf{r}},t)\|_2^2 \\ & + \lambda_1\|K_{trans}(\mathbf{r})\|_{TV} + \lambda_2\|K_{trans}(\mathbf{r})\|_1 \end{aligned} \tag{9}$$

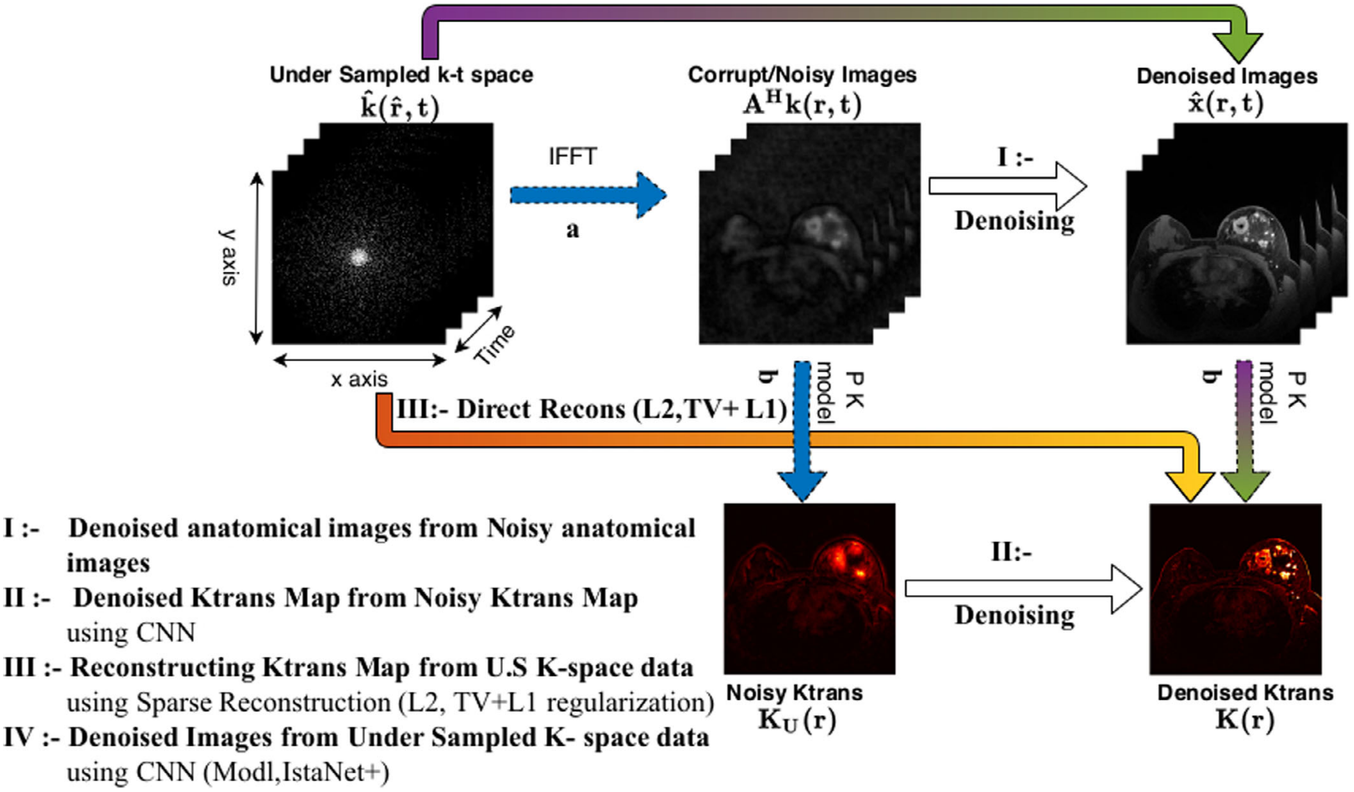

FIG. 2. This figure shows the methods for TK parameter estimation from undersampled k-t space data. **I** represents estimating anatomical images from corrupted images constructed from zero padded $\hat{\mathbf{k}}(\hat{\mathbf{r}},t)$ using IFFT (**a**). **II** represents estimating K_{trans} map from corrupted map which is constructed using zero padded $\hat{\mathbf{k}}(\hat{\mathbf{r}},t)$ using the Patlak model (**b**). **III** represents direct reconstruction of K_{trans} map from $\hat{\mathbf{k}}(\hat{\mathbf{r}},t)$ using model-based iterative schemes for sparse reconstruction. **IV** represents construction of high quality anatomical images from $\hat{\mathbf{k}}(\hat{\mathbf{r}},t)$ using Deep Learning, which in turn can be utilized to find TK parameters. [Color figure can be viewed at wileyonlinelibrary.com]

$$v_p(\mathbf{r}) = \underset{v_p}{\operatorname{argmin}} \|f(v_p) - \hat{\mathbf{k}}(\hat{\mathbf{r}},t)\|_2^2 + \lambda_3\|v_p(\mathbf{r})\|_{TV} + \lambda_4\|v_p(\mathbf{r})\|_1 \tag{10}$$

Each equation was solved independently using limited memory Broyden-Fletcher-Goldfarb-Shanno (l- BFGS) algorithm[33] and gradients were calculated in similar fashion as in Ref. [19] by relaxing the norm[34]. The pipeline of this method with and without regularization is summarized in Fig. 2 as method **III** in which $L2$ denotes solving Eq. (7) alone.

3.B. Indirect Parametric Reconstruction using sparse recovery methods

For indirect reconstruction, experiments were also performed using $\|\cdot\|_{TV}$ and $\|\cdot\|_1$ as regularization terms as shown in Eq. (11) to induce sparsity, where $\|\cdot\|_{TV}$ is anisotropic TV norm. This algorithm first reconstructs the anatomical images from undersampled k-space data using these regularization terms. Subsequently, these anatomical images through Patlak model provide estimation of K_{trans} map. This method was tested for two patients to compare the performance with direct parametric reconstruction methods as well as indirect DL methods discussed in this work. The iterative reconstruction utilized l-BFGS technique in the optimization. The cost-function can be written as

$$s(\mathbf{r},t) = \underset{s(\mathbf{r},t)}{\operatorname{argmin}} \|U(\hat{\mathbf{r}},t) * F(s(\mathbf{r},t)) - \hat{\mathbf{k}}(\hat{\mathbf{r}},t)\|_2^2 + \lambda_1\|s(\mathbf{r},t)\|_{TV} + \lambda_2\|s(\mathbf{r},t)\|_1 \tag{11}$$

3.C. ISTA-Net$^+$

ISTA-Net$^+$ [26] is a DL implementation of iterative shrinkage threshold algorithm (ISTA).[26] In this implementation, unrolling the number of iterations and stacking them as individual blocks (phases) of the neural network was performed. ISTA is a popular method for solving the CS problem such as Eq. (12).

$$\hat{\mathbf{x}} = \underset{x}{\operatorname{argmin}} \|\mathbf{A}\mathbf{x} - \mathbf{b}\|_2^2 + \theta\|\Gamma\mathbf{x}\|_1 \tag{12}$$

In the current problem of CS Dynamic MRI, the matrix A represents the undersampling Fourier transform matrix that is, $\mathbf{A} = U(\hat{\mathbf{r}},t) * F(\cdot)$, $\mathbf{b} = \hat{\mathbf{k}}(\hat{\mathbf{r}},t)$, θ is the Lagrangian multiplier and Γ is the domain transfer function. This problem is solved using proximal gradient method as shown below in Eqs. (13) and (14).

$$\mathbf{r}^k = \mathbf{x}^{k-1} - \rho^k\mathbf{A}^{\mathbf{H}}(\mathbf{A}\mathbf{x}^{k-1} - \mathbf{b}), \tag{13}$$

$$\mathbf{x}^k = \underset{x}{\operatorname{argmin}} \frac{1}{2}\|\mathbf{r}^k - \mathbf{x}\|_2^2 + \theta^k\|\Gamma x\|_1 \tag{14}$$

Here ρ^k denotes the step size of the steepest descent at each iteration k. In Ref. [26] Eq. (14) was solved by approximating $\mathbf{x}^k = \mathbf{r}^k + \mathbf{w}^k$ where $\mathbf{w}^k$ is the high-pass value and is related to $\mathbf{x}^k$ by relation $\mathbf{w}^k = \mathcal{G}^k \circ \mathcal{D}^k(\mathbf{x}^k)$, and both $D^k(\cdot)$ & $G^k(\cdot)$ are implemented using a convolutional neural network (CNN) at every iteration k . Using this relation and denoting the domain transfer function Γ by $\mathcal{H}(\cdot)$, Eq. (14) can be modified as Eq. (15)

$$\mathbf{x}^k = \underset{\mathbf{x}}{\operatorname{argmin}} \frac{1}{2}\|\mathcal{H}^k(\mathcal{D}^k(\mathbf{x})) - \mathcal{H}^k(\mathcal{D}^k(\mathbf{r}^k))\|_2^2 + \theta^k\|\mathcal{H}^k(\mathcal{D}^k(\mathbf{x}))\|_1 \tag{15}$$

Note that $\tilde{\mathcal{H}}^k$ is the left inverse of $\mathcal{H}^k$, such that $\tilde{\mathcal{H}}^k \circ \mathcal{H}^k = \mathcal{I}$. Using these relations the solution of Eq. (15) simplifies to

$$\mathbf{x}^k = \mathbf{r}^k + \mathcal{G}^k(\tilde{\mathcal{H}}^k(soft(\mathcal{H}^k(\mathcal{D}^k(\mathbf{r}^k)), \theta^k))) \tag{16}$$

In the network, the parameters belong to a set Θ such that $\Theta = \{\rho^k, \theta^k, \mathcal{D}^k, \mathcal{G}^k, \mathcal{H}^k, \tilde{\mathcal{H}}^k\}_{k=1}^N$ are trainable parameters, where N is the number of iterations (phases) in unrolled network. The loss function for this CNN was defined as

$$\mathcal{L}(\Theta) = \frac{1}{N_b}\Sigma_{i=1}^{N_b}\|\mathbf{x}_i^N - \hat{\mathbf{x}}_i\|_2^2 + \frac{C}{NN_b}\Sigma_{i=1}^{N_b}\Sigma_{k=1}^{N}\|\tilde{\mathcal{H}}^k(\mathcal{H}^k(\mathbf{x}_i^k)) - \hat{\mathbf{x}}_i\|_2^2 \tag{17}$$

where N_b is the number of images in the batch, C is an constant to give weightage to the second term, $\{\mathbf{b}_i, \mathbf{x}_i\}_{i=1}^M$ are the input & label pair and M is the size of training set. The architecture of ISTA-Net$^+$ is shown in Fig. 3.

3.D. MODL

MODL stands for MOdel-based reconstruction using DL prior and was proposed in Ref. [27]. It is inspired from plug and play[35] methods for model-based reconstruction which formulates the optimization equation as follows:-

$$\mathbf{x}^k = \underset{\mathbf{x}}{\operatorname{argmin}} \underbrace{f(\mathbf{x})}_{\text{Constraint}} + \lambda \underbrace{g(\mathbf{x})}_{\text{prior}} \tag{18}$$

For CS recovery in dynamic MRI (which is the problem at hand), the formulation is as follows:

$$\mathbf{x}^k = \underset{\mathbf{x}}{\operatorname{argmin}} \underbrace{\frac{1}{2}\|\mathbf{A}\mathbf{x} - \mathbf{b}\|_2^2}_{\text{Constraint}} + \lambda \underbrace{\|\mathcal{N}_w(\mathbf{x})\|_2^2}_{\text{prior}} \tag{19}$$

where $\mathbf{A}$ is the undersampling fourier transform and $\mathcal{N}_w$ is the prior of the noise and is given by $\mathcal{N}_w(\mathbf{x}) = \mathbf{x} - \mathcal{D}_w^k(\mathbf{x})$. The optimization process is as given below: Eqs. (20) and (21), where Eq. (21) was solved using conjugate gradient (CG) and Eq. (20) was solved using a neural network in which $\mathcal{D}^k$ and λ^k are trainable parameters.

$$\mathbf{z}^k = \mathcal{D}_w^k(\mathbf{x}^k) \tag{20}$$

$$\mathbf{x}^{k+1} = (\mathbf{A}^{\mathbf{H}}\mathbf{A} + \lambda\mathbf{I})^{-1}(\lambda\mathbf{z}^k + \mathbf{A}^{\mathbf{H}}\mathbf{b}) \tag{21}$$

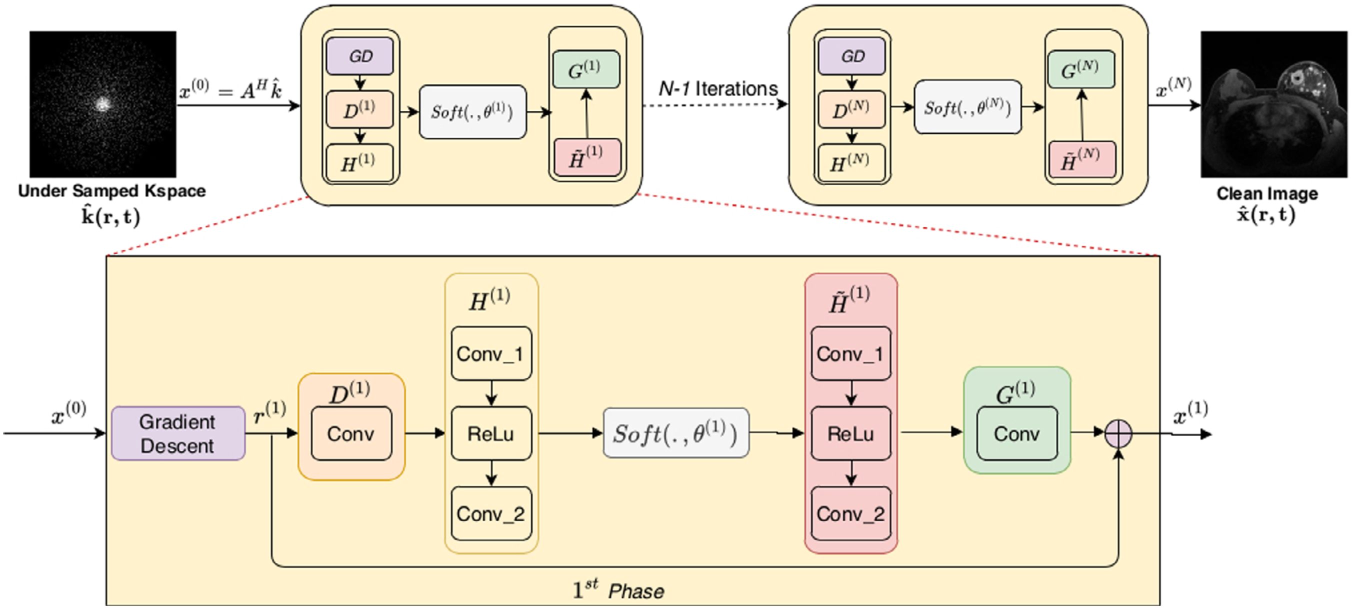

FIG. 3. Network architecture of ISTA-Net$^+$ expanded to show 1st iteration (phase) where $\{\rho^{(1)}, \theta^{(1)}, \mathcal{D}^{(1)}, \mathcal{G}^{(1)}, \mathcal{H}^{(1)}, \tilde{\mathcal{H}}^{(1)}\}$ are the trainable parameters in 1st phase. The description of the same is provided in Section 3.C. In here, "Conv" stands for convolution filter. [Color figure can be viewed at wileyonlinelibrary.com]

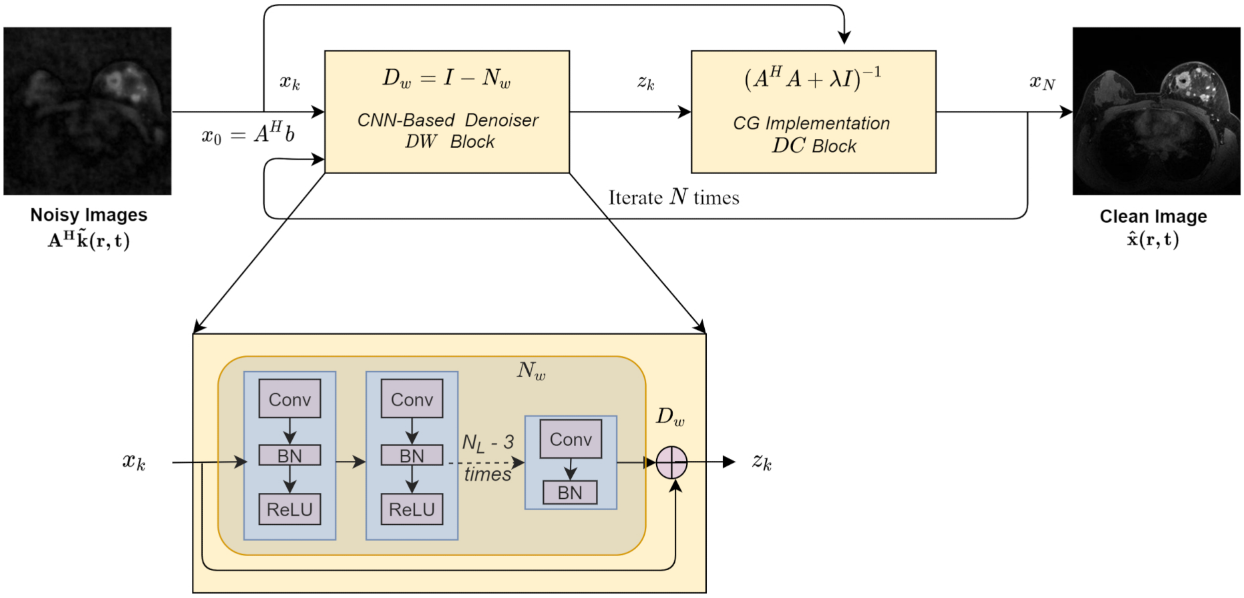

FIG. 4. Network architecture of MODL showing N iterations(phases) in rolled fashion. In the figure Conv. stands for Convolution filter, DC stands for Data Consistency block and DW stands for Denoising block. Each iteration in the network consists of two blocks, DC block and DW block, the expanded view of DW block is shown below, which consists of $N_L - 1$ layers of Conv. filters, BN (Batch Normalization) layer and ReLu layer and one layer of Conv. filters and BN layer. The description of MODL is given in Section 3.D. [Color figure can be viewed at wileyonlinelibrary.com]

It has been demonstrated that sharing the weights across all iterations(phases) give superior performance and requires less training time and data.[27] MODL network architecture is given in Fig. 4 in a rolled fashion. Each iteration of the network consists of a Denoising block (*DW*) and a Data Consistency block (*DC*), which utilizes CNN and CG, respectively. The *DW* block consists of N_L layers out of which $N_L - 1$ layers each having 2D Convolutional (Conv) filters, a batch normalization layer (BN) and a ReLU layer. The last layer in each *DW* contained only 2D convolutional filters and a BN layer.

4. EXPERIMENTAL DETAILS

4.A. Dataset

For all experiments performed in this work, QIN Breast DCE-MRI dataset[36] was utilized which is publicly accessible and is available on The Cancer Imaging Archive (TCIA).[37] It contains breast DCE-MRI images from a longitudinal study to assess the breast cancer response to neoadjuvant chemotherapy (NACT).[38] Images were acquired at two points: prior to first round of treatment (V1) and post first round (V2). The images were acquired using Siemens 3T system with a body coil and a four-channel bilateral phased-array breast coil. The DCE-MRI images are fat-saturated and were acquired using 3D gradient echo-based TWIST (Time-resolved angiography With Stochastic Trajectories) sequence.[39] The data acquisition parameters included flip angle of ten°, Time to echo (TE), and Time of repetition (TR) of 2.9 and 6.2 ms, respectively, field of view (FOV) of 30-34 cm, 320 × 320 in-plane matrix size and a slice thickness of 1.4 mm. There are 28-32 image volumes each containing 120-128 slices with temporal resolution of 18–20 s and total acquisition time of ~ 10 min. A Gadolinum-based contrast agent Gd-HP-D03A [trade name: ProHance] was administered with a dose of 0.1 mmol/kg of body mass followed by 20 ml saline flush at a speed of 2 ml/s using a programmable injector. The data that was utilized in this work included V1 and V2 studies of ten patients. Data for more patients with scans after more treatment cycles is available[40] and was discussed in detail in Ref. [41]. However, the data does not meet the recommended practise guidelines of American Society of Radiology for DCE-MRI of the breast.[42] The dataset provided did not utilize fat suppression as recommended and also does not satisfy the requirements of in-plane and slice thickness recommendations (1 and 3 mm as per standard). Hence this dataset was not utilized in this work.

4.B. Implementation

Data from ten patients was retrospectively undersampled in the k-t space with undersampling rates ($\mathbf{R}$) of 20×, 50×, and 100× with the sampling patterns or masks ($U(\hat{\mathbf{r}}, t)$) generated by randomized golden-angle radial scheme.[17] The AIF was assumed to be the population average with delay time as specified in the patient's metadata. The K_{trans} maps generated from undersampled data with zero padding (without CS techniques), suffer from loss of high frequency details as shown in Fig. 5, these maps are labeled as noisy K_{trans} maps. From the undersampled k-t space data $\hat{\mathbf{k}}(\hat{\mathbf{r}}, t)$, our aim is to generate the K_{trans} map using methods mentioned in Section 3 via Patlak model.[9] The details of implementation of each method are given below and are summarized in Table I.

TABLE I. Summary of reconstruction methods utilized in this work.

Method	Iterative Parametric Reconstruction	Deep Learning (DL)
Direct	Deployed for all ten subjects data. [**Referred as** '**Direct** $TV + L1$']	Not performed as method is not generic to deploy for varying number of time points and image size. More training data are required.
Indirect	Deployed on two subjects to demonstrate better performance of direct parametric reconstruction. method [**Referred as** '**Indirect** $TV + L1$']	Deploys generic DL-based (iterative) reconstruction methods and is trainable with very less data (in here with five patients data). Tested on five patients data. [**Referred as** **"DL" (ISTA and MODL)**]

4.B.1. Direct reconstruction

As discussed in Section 3.A., the direct reconstruction method was deployed with $\|\cdot\|_{TV}$ and $\|\cdot\|_1$ regularization and without any regularization (abbreviated as $TV + L1$ and $L2$, respectively). The regularization parameters $\{\lambda_1, \lambda_2, \lambda_3, \lambda_4\}$ shown in Eqs. (9) and (10) were selected on the basis of reconstruction performance on a single patient and were generalized for all patients for the given undersampling rate. For all experiments, the number of iterations were fixed as ten as the cost function variation beyond ten iterations was not significant. For comparison, we also generated the map directly from undersampled k-t space data using zero padding and these results were reported as undersampled map.

4.B.2. Indirect parametric reconstruction

Indirect parametric reconstruction using $\|\cdot\|_{TV}$ and $\|\cdot\|_1$ was performed on two patients to compare the performance of indirect iterative technique with direct parametric technique as well as indirect deep learning-based technique. The method was discussed in Section 3.B. The regularization parameters λ_1 and λ_2 were determined in a similar manner as for direct iterative methods.

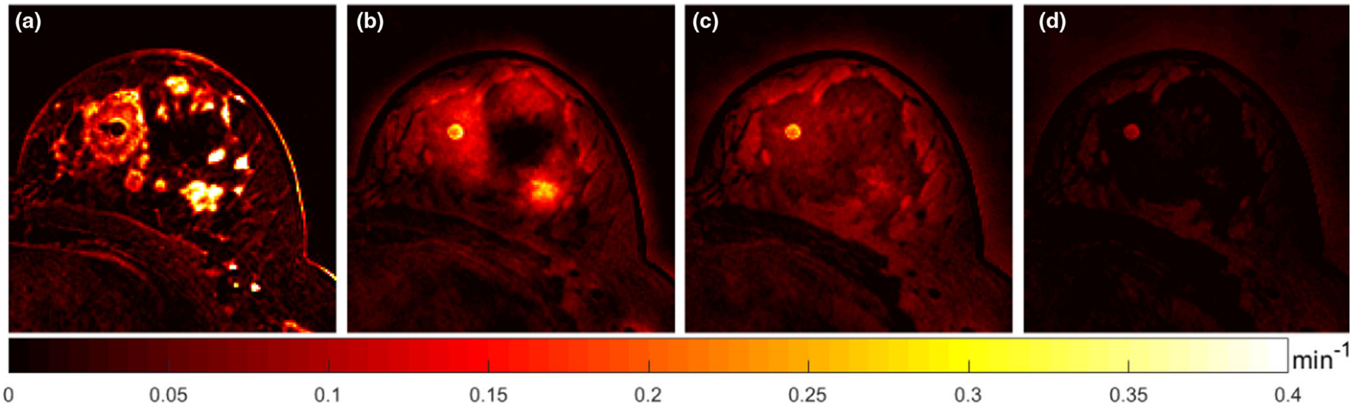

FIG. 5. K_{trans} maps reconstructed using zero padding (a) fully sampled k-t space data; undersampling rate, $\mathbf{R}$, being (b) 20×, (c) 50×, and (d) 100×. [Color figure can be viewed at wileyonlinelibrary.com]

4.B.3. ISTA-Net$^+$

For all under-sampling rates (**R**), the number of phases N are fixed to 11. ADAM[43] was used for optimization as this scheme maintains two learning rates corresponding to each parameter. These learning rates are estimated from the first and second moments of the gradients. The size and number of filters (shown in Fig. 3) are provided in Table II and were kept constant for all values of **R**. ISTA-Net$^+$ also learns the step size ρ^k and regularization parameter θ^k for each phase. There are no bias parameters in this network. For each **R**, the network was trained from scratch for 100 epochs with batch-size of 8, using the loss function as shown in Eq. (17). The learning rate was 10^{-4} and other parameters for ADAM were $\beta_1 = 0.9$, $\beta_2 = 0.999$, and $\epsilon = 10^{-8}$. We divided the dataset into training and testing at the patient level. Five of them were utilized for training and another five for testing making sure that no two images from the same patient were utilized for both training and testing. For training ISTA-Net$^+$ (and MODL), total of 4,000 ($n_z = 40$, $n_t = 10$) 2D images from both V1 and V2 data of five patients were selected as training data and 400 images were utilized for validation. Here n_z stands for number of axial slice and n_t stands for number of dynamic acquisitions. ISTA-Net$^+$ was trained for MRI reconstruction from undersampled data using 100 (360 for MODL) images[26] hence our data were 40× (≃11× for MODL) the training data used in base paper and deemed to be sufficient for this task. The input-label pair for training the network is $\mathcal{T} = \{\{\hat{\mathbf{k}}(\hat{\mathbf{r}}, t), U(\hat{\mathbf{r}}, t)\}_i, \mathbf{s}_{\mathrm{i}}(\mathbf{r}, t)\}_{i=1}^{M}$ where $U(\hat{\mathbf{r}}, t)$ stands for the undersampling mask. To incorporate the information in complex domain of $A^H\hat{\mathbf{k}}(\hat{\mathbf{r}}, t)$, we utilized the modulus (absolute value) of steepest descent estimate $\mathbf{r}^k$ calculated from Eq. (13). For testing, anatomical images of all slices containing ROI of five patients were utilized in which 3248 two-dimensional slices (resulting in 220 K_{trans} maps) were present in total. As mentioned earlier, the testing set corresponds to different patient data than the training set. From these anatomical images, K_{trans} maps were generated using Patlak model. The total number of trainable parameters in ISTA-Net$^+$ for 11 phases are 411 862 and it took ≃ 18 h to train with each epoch taking ≃ 11 mins. Reconstruction time for a single anatomical image was ≃ 42 ms.

Table II. Size of filters $N_x \times N_y$, number of channels N_c and the number of filters N_f at each layer of a phase (k) for ISTA-Net$^+$ as shown in Fig 3.

Filter Name		Size of filter (N_xxN_yxN_cxN_f)
$D^{(k)}$		3×3×1×32
$H^{(k)}$	Conv_1	3×3×32×32
	Conv_2	3×3×32×32
$\tilde{H}^{(k)}$	Conv_1	3×3×32×32
	Conv_2	3×3×32×32
$G^{(k)}$		3×3×32×1

These hyperparameters were same were same for all phases/iterations (k), although weights were not shared.

4.B.4. MODL

For training MODL network, the training, validation, and testing dataset were same as ISTA-Net$^+$. The trainable parameters were shared among all layers and the iterations of CG were performed till change in residue was less than 10^{-4}. The number of iterations (N) were 11 for **R** of 20× and 15 for **R** of 50× and 100×. The number of layers (N_L) were kept as five in all cases and the filter size and number of filters that were deployed are given in Table III. MODL also learns the regularization parameter λ shown in Eq. (19). The real and complex components of the $\mathbf{A}^H\hat{\mathbf{k}}(\hat{\mathbf{r}}, t)$ were taken as separate channels in input to the neural network. For each **R**, the network was trained initially with $N = 1$ for 100 epochs. These trained parameters were used to initialize networks with $N = 11$ (for **R** = 20×) and $N = 15$ (for **R** = 50× and 100×) and further trained for 50 epochs with batch size of 4. ADAM optimizer was used for training MODL and mean squared error between label and output was taken as loss function. The learning rate was 10^{-3} and the parameters for ADAM were $\beta_1 = 0.9$, $\beta_2 = 0.999$ and $\epsilon = 10^{-8}$. The total number of trainable parameters in MODL are 113,921 and it took ≃ 25 hrs to train for $N = 10$ and ≃ 36 hrs for $N = 15$. It took ≃ 140 ms to reconstruct one anatomical image for $N = 10$ and ≃ 160 ms to reconstruct for $N = 15$.

4.B.5. Computational implementation

All computations were carried out on a Linux workstation with Intel i9 processor with 2.10 GHz clock speed, having 128 GB RAM and a Quadro RTX 8000 GPU with 48 GB memory. Pre-processing and Post-processing steps were performed in MATLAB and both neural networks were implemented in Tensorflow v1.13. The direction reconstruction algorithm was implemented on MATLAB 2018b using parallel computing toolbox on eight threads. Implementation of the proposed method including the developed code was made available as open-source at https://github.com/Medical-Imaging-Group/DCE-MRI-Compare.

4.C. Figures of merit

For comparing the performance of the above mentioned methods, four figures of merit (metrics) were utilized namely,

Table III. Size of filters $N_x \times N_y$, number of channels N_c and the number of filters N_f at every layer in DW block of k^{th} iteration for MODL as shown in Fig 4.

Layer no.	Size of filter (N_xxN_yxN_cxN_f)
1	3×3×2×64
2 - 4	3×3×64×64
5	3×3×64×2

These hyperparameters were same for all phases/iterations and the weights were also shared.

PSNR (peak signal-to-noise-ratio), normalized Root-Mean-Square-Error (nRMSE), Structural Similarity Index Measure (SSIM), [44] and a modification of Xydeas[45] metric. The nRMSE is RMSE, divided by the 90th percentile value of K_{trans} in the ROI of reference image (ground truth, in here reconstructed K_{trans} using fully sampled data) as the 90th percentile of K_{trans} value has been found as a clinically significant biomarker for tumor.[46] The lower the value, the better is performance of the method under consideration. Xydeas metric measures the edge information that is present in each pixel and compares the magnitude and orientation of the edges in the reference and test image. In case of this metric, higher value represents better performance of the method. The PSNR $\in (0,\infty)$ (measured in dB), is the measure of signal compare to noise present in the reconstructed K_{trans}, higher value represent better reconstructed K_{trans}. SSIM & Xydeas metric $\in (0,1]$ and they take value 1 when both images are same. nRMSE $\in [0,\infty)$ and the value is 0 when both images are exactly same.

4.C.1. Statistical test

We conducted t-test for unequal variance (also known as Welch test). The null hypothesis was that TV + L1 and deep learning-based methods have same mean performance for PSNR and SSIM. We only performed statistical test on DL and $TV + L1$ as it is evident from the results that $TV + L1$ always outperform $L2$ and, therefore, only the best method of direct iterative technique was compared with indirect DL-based methods. Welch test was conducted for PSNR and SSIM separately for $\mathbf{R} = 20\times$, $50\times$ and $100\times$ for each of five patients. Xydeas metric was not used for statistical test as it only conveys the information about edges and not the whole image. Similarly nRMSE was not utilized for this test as it just a scaled form of PSNR ($\text{PSNR} = 20\log\frac{\max}{\text{mse}}$). The number of observations for each patient were the number of slices having the tumor. Significance level of 0.05 was selected for testing and was modified using Šidák[47] correction to ≃ 0.01 for testing on five patients data. The results were shown in Table IV for Welch test in whole breast region and in Table V for the ROI. Negative "t-stat" shows that DL performed better than TV + L1 and Positive *t*-stat shows the opposite. "*P*" value of < 0.01 shows significant difference in the performance of two methods. Columns "TV/DL" shows whether TV L1 or DL has performed better in that patient for that metric. TV + L1 performs better if "t-stat" >0 and DL performs better if "t-stat" < 0. "Sig ?" denotes if the difference is significant to reject the null hypothesis ($P < 0.01$) or not.

5. RESULTS

The reconstructed K_{trans} map for the mentioned undersampling rates (**R**) using the methods described earlier were presented for two representative cases, patients "A" and "B" in Figs. 6 and 9, respectively. These figures present the K_{trans} map generated from fully sampled data, undersampled data with zero padding and using direct (iterative CS scheme) and indirect deep learning-based reconstruction techniques. For indirect reconstruction, as mentioned earlier, $\|\cdot\|_{TV} + \|\cdot\|_1$ regularization was utilized. For model-based direct reconstruction, no regularization ($L2$), and $\|\cdot\|_{TV} + \|\cdot\|_1$ regularization were used and for indirect deep learning-based reconstruction (deep learning, DL-based), ISTA-Net$^+$ (ISTA) and MODL were used to reconstruct the anatomical images, which were later used to estimate the map. Figures 8 and 11 shows the performance of these methods for these patients "A" and "B", respectively, in terms of the metrics mentioned in subsection 4.C. The abbreviation 20×, 50×, and 100× was utilized to denote respective rates of undersampling (**R**). In Fig. 12, the average performance of these methods on the test dataset from five patients which consists of multiple samples from multiple patients as mentioned in Section 4.A. was presented. No sample from either V1 or V2 volume for these five patients were present in training set. From here onward,

Table IV. Table showing t-test results for the whole breast region of five patients for **R**= 20×, 50×, 100×.

		R = 20×				R = 50×				R = 100×			
Pat No.	Metric	t-stat	P	TV/ DL	Sig?	t-stat	P	TV/ DL	Sig?	t-stat	P	TV/ DL	Sig?
A	PSNR	−4.23	$3.1e^{-4}$	DL	Yes	−0.42	0.67	DL	No	2.97	0.0065	TV	Yes
	SSIM	−3.01	0.0058	DL	Yes	3.51	0.0019	TV	Yes	6.61	$6.1e^{-6}$	TV	Yes
B	PSNR	−2.11	0.048	DL	No	5.01	$5.2e^{-5}$	TV	Yes	7.95	$6.6e^{-8}$	TV	Yes
	SSIM	−0.91	0.37	DL	No	6.58	$3.52e^{-6}$	TV	Yes	12.39	$2.7e^{-9}$	TV	Yes
C	PSNR	2.73	0.014	TV	Yes	6.03	$1.1\ e^{-5}$	TV	Yes	8.54	$3.8\ e^{-7}$	TV	Yes
	SSIM	12.35	$1.5\ e^{-8}$	TV	Yes	7.15	$5.3\ e^{-5}$	TV	Yes	8.65	$1.2\ e^{-5}$	TV	Yes
D	PSNR	−4.07	$6.5e^{-4}$	DL	Yes	−0.27	0.79	DL	No	1.16	0.26	TV	No
	SSIM	4.13	$3.5e^{-4}$	TV	Yes	6.58	$5.6\ e^{-7}$	TV	Yes	10.71	$2.1\ e^{-10}$	TV	Yes
E	PSNR	−3.93	0.0023	DL	Yes	0.29	0.77	TV	No	4.62	$1.3e^{-4}$	TV	Yes
	SSIM	9.96	$2.1\ e^{-9}$	TV	Yes	13.62	$8.6\ e^{-13}$	TV	Yes	16.25	$5.1\ e^{-10}$	TV	Yes

The t-test was performed for two metrics PSNR and SSIM. Negative "t-stat" shows that DL performed better than direct TV + L1 (abbreviated as TV in this table) and positive t-stat shows the opposite. "P" value of < 0.01 shows significant difference in the performance of two methods. "Sig ?" denotes if the difference is significant to reject the null hypothesis ($P < 0.01$) or not. Description of these are given in Section 4.C.1.

Table V. Table showing t-test results for the ROI of five patients for **R**= 20×, 50×, 100×.

		R = 20×				R = 50×				R = 100×			
Pat No.	Metric	t-stat	P	TV/ DL	Sig?	t-stat	P	TV/ DL	Sig?	t-stat	P	TV/ DL	Sig?
A	PSNR	−2.94	0.0069	DL	Yes	2.47	0.021	TV	No	3.11	0.0049	TV	Yes
	SSIM	−1.51	0.14	DL	No	6.16	4.1 e^{-6}	TV	Yes	7.36	8.1 e^{-8}	TV	Yes
B	PSNR	−2.88	0.011	DL	Yes	0.72	0.47	TV	No	4.24	3.6 e^{-4}	TV	Yes
	SSIM	1.04	0.31	TV	No	5.54	4.4 e^{-5}	TV	Yes	9.44	1.1 e^{-7}	TV	Yes
C	PSNR	0.19	0.85	TV	No	4.74	1.6 e^{-4}	TV	Yes	5.55	5.5 e^{-5}	TV	Yes
	SSIM	8.13	1.9 e^{-7}	TV	Yes	7.37	2.3 e^{-5}	TV	Yes	6.68	9.1 e^{-5}	TV	Yes
D	PSNR	−3.62	0.0021	DL	Yes	−1.46	0.16	DL	No	−0.47	0.64	DL	No
	SSIM	0.31	0.76	TV	No	5.74	7.6 e^{-6}	TV	Yes	4.98	4.8 e^{-5}	TV	Yes
E	PSNR	−3.86	0.0015	DL	Yes	−1.43	0.17	DL	No	2.47	0.021	TV	No
	SSIM	3.32	0.0046	TV	Yes	7.25	2.9 e^{-7}	TV	Yes	15.31	3.8 e^{-12}	TV	Yes

The t-test was performed for two metrics PSNR and SSIM. Negative "t-stat" shows that DL performed better than direct TV + L1 (abbreviated as TV in this table) and positive t-stat shows the opposite. "*P*" value of < 0.01 shows significant difference in the performance of two methods. "Sig ?" denotes if the difference is significant to reject the null hypothesis ($P < 0.01$) or not. Description of these are given in Section 4.C.1.

we will use $L2$ and direct $TV + L1$ as shorthand notation for model-based direct reconstruction method using no regularization and $\|\cdot\|_{TV} + \|\cdot\|_1$ regularization, respectively. The indirect TV $+L1$ for indirect $\|\cdot\|_{TV} + \|\cdot\|_1$ regularized reconstruction. Of the testing dataset, these two patients were taken as representative cases because they belong to the extreme spectrum of breast tissue inhomogeneity. Patient "A" has less dense breast than patient "B" (as patient "A" is postmenopausal) and the former also has a largest breast tumor in the dataset, whereas the tumor in latter is the smallest. Experiments using indirect $TV + L1$ was only performed in these two cases to corroborate claim in Ref. [19] that direct reconstruction perform better than indirect for higher undersampling rate and to explore the difference in results of $TV + L1$ and DL was caused due to direct vs indirect techniques or not. The results confirms that direct $TV + L1$ performs the best compared to indirect $TV+ L1$ with DL-based methods being the least performing, especially in higher undersampling rates. The detailed analysis has been presented in the next subsections.

5.A. R = 20×

5.A.1. Patient "A"

Figure 6 shows the K_{trans} map of left breast and ROI of patient "A," generated from fully sampled k-t space data of patient "A." The patient is 56 yr old and has been diagnosed with invasive ductal carcinoma (IDC). Figure 6 also shows the K_{trans} map generated using the discussed reconstruction methods as mentioned above. Figures 6(a) and 6(b) shows the map of the left breast and the ROI of the patient, respectively. Figure 7 shows the absolute difference between K_{trans} maps generated using different reconstruction techniques and map generated from fully sampled data. Figure 8 shows performance of these techniques in terms of figures of merit. For the left breast of patient, the DL methods perform better in terms of PSNR, nRMSE, and SSIM, but are surpassed by direct and indirect $TV + L1$ regularized reconstruction in terms of Xydeas metric as seen in Fig. 8(a). Same can be verified from Fig. 6(a) that although the boundaries are well-preserved in DL-based methods, the texture of tissues is lost. The results in ROI (i.e., tumor) can be seen in Fig. 8(b) in which direct $TV + L1$ performs comparable to DL in terms of SSIM as well and even $L2$ gives better results for Xydeas metric than DL. This can be attributed to loss of tissue texture in and around the tumor in the map generated using DL-based methods. In the left breast and ROI region, it can be seen that indirect $TV + L1$ is surpassed by DL for all **R** in terms of PSNR, SSIM, and nRMSE. Moreover, direct $TV + L1$ performs better than indirect $TV + L1$ in terms of SSIM and Xydeas metric for **R** = 20×.

5.A.2. Patient "B"

Figure 9 shows the K_{trans} map of right breast and ROI in patient "B," generated from fully sampled k-t space data of patient "B." The patient is 33 yr old and was diagnosed with IDC. Fig. 9 also shows the K_{trans} map generated using reconstruction methods as discussed above. Figures 9(a) and 9(b) shows the map of the right breast and in the ROI of patient, respectively. Figure 10 shows the absolute difference between K_{trans} maps generated using different reconstruction techniques and map generated from fully sampled data. Figure 11 shows performance of these techniques objectively. For the right breast of patient the DL perform better in terms of PSNR, nRMSE, and SSIM, but are surpassed by direct $TV + L1$ regularized reconstruction in terms of Xydeas metric as seen in Fig. 11(a). Same can be verified from Fig. 9(a) that although the boundaries are well-preserved in DL-based methods, the map looks smoothed. Indirect $TV + L1$ performs at par with direct $TV + L1$ but is outperformed by DL in all metrics except Xydeas. The performance in ROI (i.e., tumor) can be seen in Fig. 11(b) in which the DL outperforms

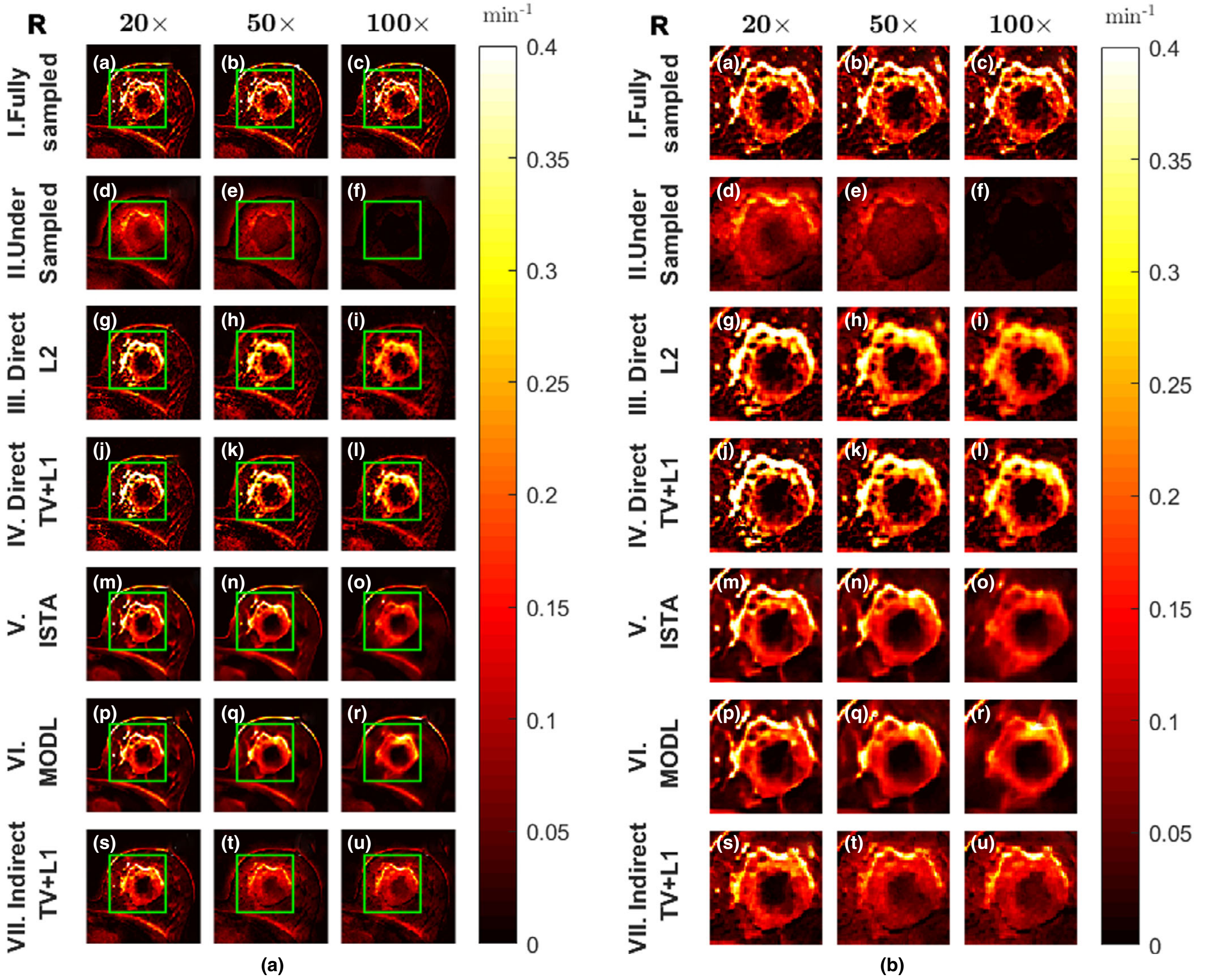

Fig. 6. Reconstructed K_{trans} map for one representative slice of (a) the left breast along with the ROI and (b) the zoomed version of ROI (green color bounded box in (a)) of patient "A." The different under-sampling rates, **R**, was given column wise. The reconstruction methods deployed row wise are I. Fully sampled data, II. Undersampled data with zero padding, III. $L2$ (no regularization)-based direct reconstruction, IV. Direct $TV + L1$ regularized direct reconstruction, V. ISTA-Net$^+$-based indirect reconstruction, VI. MODL-based indirect reconstruction and VII. Indirect TV + L1 iterative reconstruction. In (a) it can be seen that as **R** increases the details present in the map were lost, also for all **R**, direct $TV + L1$ regularization preserves edges and boundaries, whereas DL-based methods (ISTA and MODL) causes blurring of the tumor region and surrounding tissues. Meanwhile indirect $TV + L1$ causes diffusion effect at boundaries. In (b) it can be seen that direct $TV + L1$ preserves the interior and exterior boundary of the tumor and the surrounding fibrous tissues. These details were lost in DL-based reconstruction. For $L2$ based direct reconstruction, the tumor boundaries become blurry as **R** increases. [Color figure can be viewed at wileyonlinelibrary.com]

even for Xydeas metric because of small size of ROI and less soft tissue texture being present in it. In both right breast and ROI it can be seen that $L2$ reconstruction leads to specular noise in the map (visible in the region of implant), whereas $TV + L1$ was able to suppress this noise more effectively. Indirect $TV + L1$ performs better than direct $TV + L1$ in terms of PSNR and nRMSE but is outperformed by DL in all metrics.

5.A.3. *Average Results*

Figure 12 shows the average and extremum performance of all methods used for estimating the K_{trans} map, where Fig. 12(a) shows the performance in the whole breast that contains the tumor and Fig. 12(b) compares the performance in the ROI. For under-sampling rate of 20×, it can be inferred that in whole breast region, DL at average performs better in terms of PSNR and nRMSE than other methods and the results are comparable to direct $TV + L1$ for SSIM. Both direct reconstruction techniques score better in Xydeas metric although direct $TV + L1$ fairs better than $L2$. In ROI, the same trend was followed as seen for whole breast region. From Table IV, it is evident that for whole breast reconstruction, in four patients DL performs better in terms of PSNR compared to direct $TV + L1$ and for two cases in SSIM. Results for statistical test in ROI are shown in Table V, it can be seen that in terms of PSNR, DL performs better in four cases.

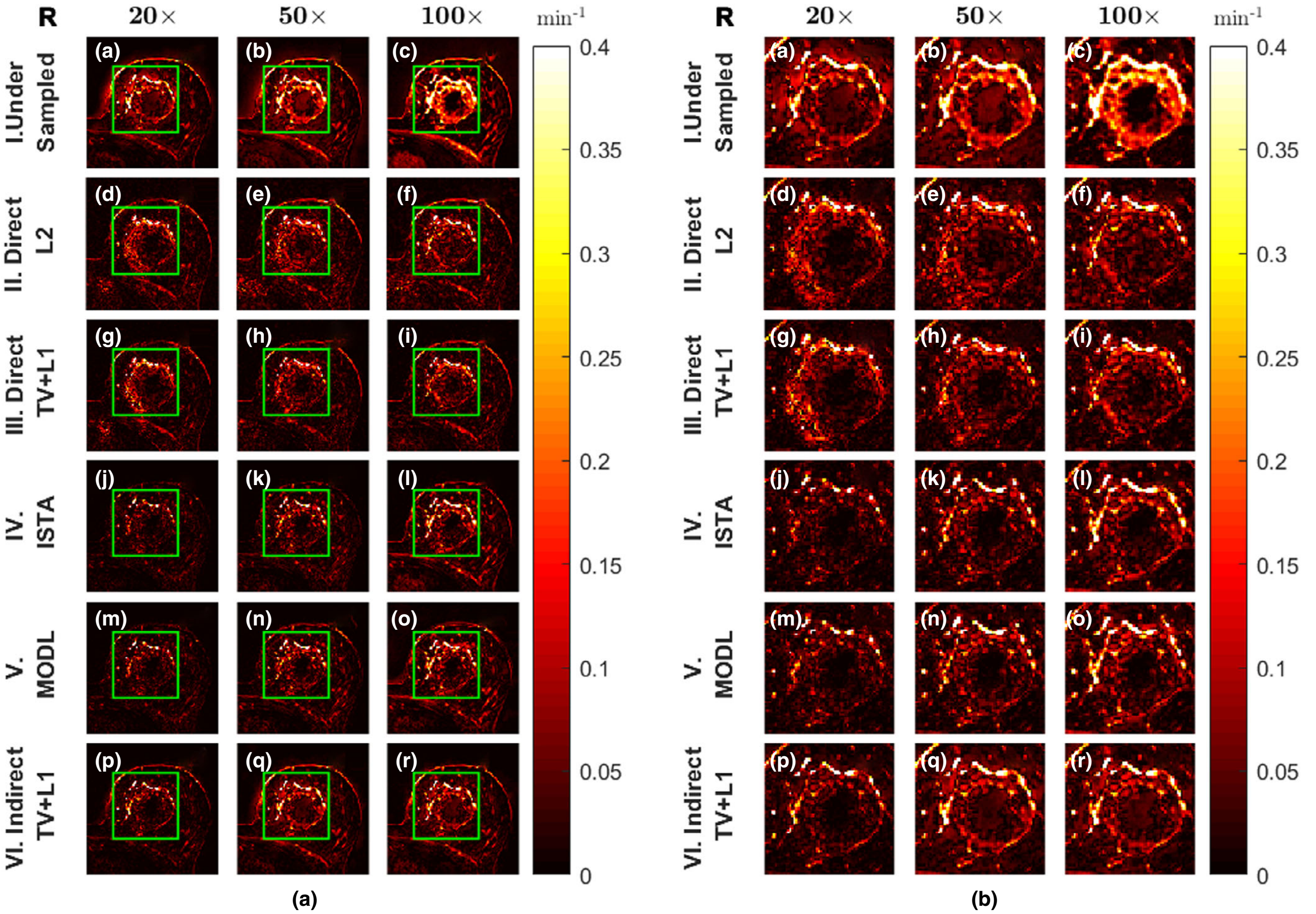

(a)

(b)

FIG. 7. Difference images between reconstructed K_{trans} map and ground truth (utilizing full data) for one representative slice of (a) the left breast along with the ROI and (b) the zoomed version of ROI (green color bounded box in (a)) of patient "A." The original reconstructed K_{trans} maps are given in Fig. 6. In (a) it can be seen that as **R** increases the details present in the map were lost, also for all **R**, direct $TV + L1$ has less loss of information on edges and in fibrous tissues surrounding tumor that DL-based methods. Meanwhile indirect $TV + L1$ have large errors at boundaries. In (b) it can be seen that direct $TV + L1$ preserves the interior and exterior boundary of the tumor and the surrounding fibrous tissues. These details were lost in DL-based reconstruction. It can also be seen that indirect $TV + L1$ has error in estimating K_{trans} in surrounding regions of the tumor. [Color figure can be viewed at wileyonlinelibrary.com]

5.B. R = 50×

5.B.1. Patient "A"

From Figs. 6 and 8, it can be seen that as **R** increases, more information was lost in the map in both left breast and ROI. In latter, one can observe that for the breast region, DL methods (IstaNet^{+} and MODL) comparable in terms of PSNR and nRMSE, while direct $TV + L1$ and $L2$ performs comparable or better in other metrics. Moreover, both direct $TV + L1$ and DL outperform indirect $TV + L1$ in all metrics. In ROI, the results are similar to that of left breast region except for the better performance of direct $TV + L1$ in all figures of merit. Both direct $TV + L1$ and DL perform better than indirect $TV + L1$ in all metrics. It can be seen from Fig. 6(b) that maps indirectly estimated using DL methods have lost more texture and the boundaries appear to be blurred. In $L2$ estimation of the map some texture within the tumor boundary was lost and for direct $TV + L1$, one can observe the staircase effect within the tumor boundary (top boundary of the tumor).

5.B.2. Patient "B"

From Figs. 9 and 11 the same trend of loss of details as **R** increases was noticed. From latter, it can be seen that in the right breast region, for all figures of merit, direct $TV + L1$ performs better than rest while results from DL methods are comparable in terms of SSIM. In Fig. 9(a), for undersampling rate of 50×, the specular noise in $L2$ increases, and in maps generated from DL methods there is further loss of texture in surrounding tissues. Moreover, the thoracic wall is not as clear in maps generated from the latter. In ROI, DL performs comparable to direct $TV + L1$ in terms of PSNR, but is outperformed by latter in rest metrics. Also, DL performs better than indirect $TV + L1$ in terms of SSIM, PSNR, and nRMSE. $L2$ also outperforms DL in terms of SSIM and Xydeas metric Fig. 9(b), the wall on which the tumor rest and surrounding tissues are blurred by DL methods, however, the shape of the tumor is better preserved in terms of outer and inner boundary. The $L2$ and direct $TV + L1$ regularized methods suffer from staircase effects at boundary but are able to preserve the

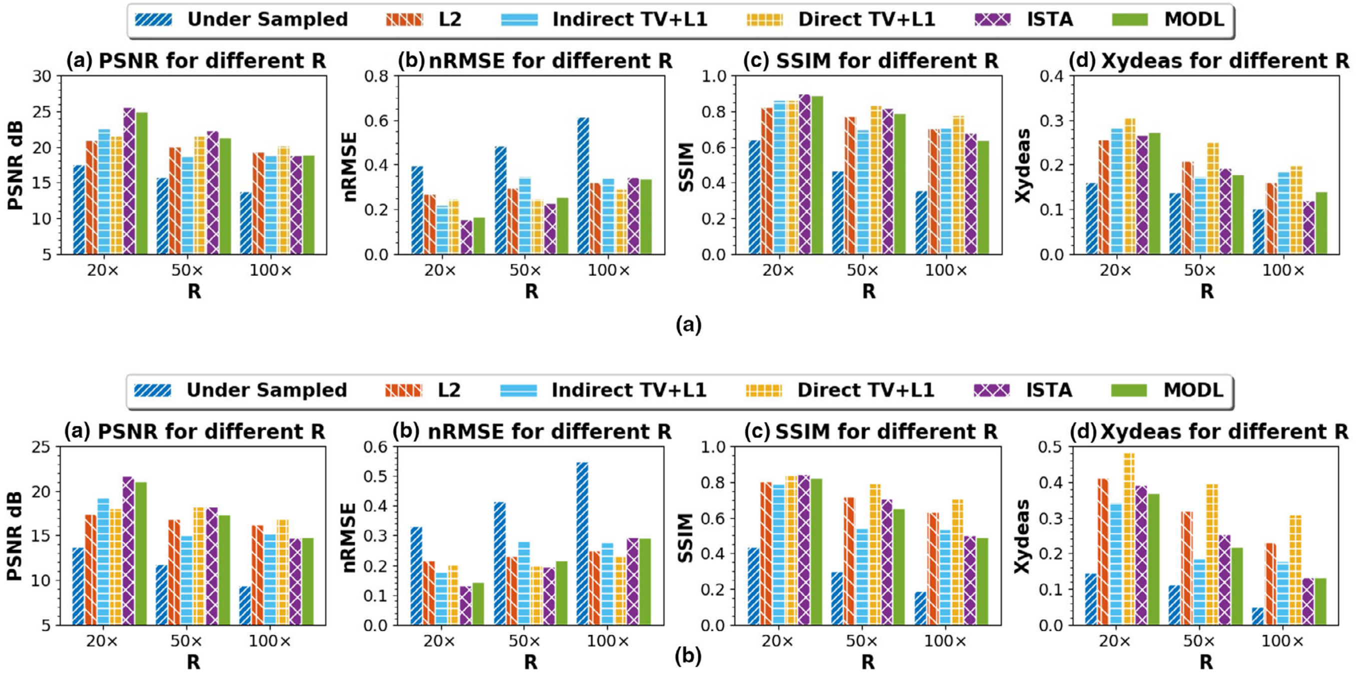

Fig. 8. Comparison of figures of merit, as discussed in Section 4.C., using different reconstruction methods presented in Section 3 for patient "A" (representative images are given in Fig. 6), in (a) left breast and (b) in ROI. In (a) For R (undersampling factor) being 20×, DL- based methods perform better in terms of PSNR, nRMSE, and SSIM while both $TV + L1$ regularized methods performs better in conserving edges. Indirect $TV + L1$ also performs better than direct methods in terms of PSNR. For higher **R** values, direct $TV + L1$ performs comparable or better than DL methods and indirect $TV + L1$ method. For 100× $L2$ performs comparable to or better than DL methods and indirect $TV + L1$. For all **R**, DL-based indirect method performs better than indirect $TV + L1$ in PSNR and SSIM. In (b) DL outperforms other techniques for 20× except for SSIM and Xydeas metric. For 50× and 100×, direct $TV + L1$ gives best results in all metrics and for 100× $L2$ outperforms DL as well. Overall, for 20×, DL-based methods perform better, whereas, for 50× and 100×, direct $TV + L1$ regularization provides improved performance. Here also indirect DL performs better than indirect $TV + L1$ in terms of PSNR and SSIM for all **R**. [Color figure can be viewed at wileyonlinelibrary.com]

soft tissue structures around the tumor including the wall on which the tumor rests. In ROI, DL performs better than indirect $TV + L1$ in terms of SSIM, PSNR, and nRMSE as well, while the latter performs better than direct method in terms of Xydeas metric.

5.B.3. Average results

From Fig. 12(a), it can be inferred that in the whole breast region, the performance of direct $TV + L1$ is best compared to other methods while DL performs close to the former in metrics other than Xydeas in which $L2$ also performs better than DL. In ROI direct $TV + L1$ outperforms other reconstruction methods and $L2$ performs close to or better than DL as shown in Fig. 12(b). From Table IV, it is clear that in terms of PSNR, direct $TV + L1$ outperforms DL in three cases but the difference is significant in only two. Moreover, in terms of SSIM, direct $TV + L1$ performs significantly better in all five cases. From Table V, it can be seen that in terms of PSNR direct $TV + L1$ outperforms DL in three cases and significantly in one. In terms of SSIM, it performs significantly better in all five cases.

5.C. R = 100×

5.C.1. Patient "A"

From Fig. 8, it can be seen that for 100×, in the left breast region $TV + L1$ regularized reconstruction performs better than other methods in all metrics. While DL performs comparable to direct $TV + L1$ in terms of PSNR and nRMSE, $L2$ performs at par or better than DL-based methods. Moreover, DL performs better than indirect $TV + L1$ in terms of PSNR and nRMSE, whereas the results are comparable in terms of SSIM. In Fig. 6(a) the loss of texture in DL-based methods are more pronounced and even the thoracic wall is not clearly visible. In the ROI direct $TV + L1$ and $L2$ provide improved performance compared to DL-based methods in all metrics, while direct $TV + L1$ outperforms $L2$ as shown in Fig. 8(b). Same can be inferred from Fig. 6(b) in which for 100× most of the high-frequency information in the map was lost in DL-based reconstruction and even the inner and outer boundaries of the tumor appear blurry. Direct $TV + L1$ preserves the boundaries and high-frequency details better than other methods, but suffers from staircase effect. The $L2$-based regularization performs better in preserving boundaries and surrounding tissues compared to DL, it blurs the region between the outer and inner boundary of the tumor. From Fig. 8(b) it can be seen that DL performs better than indirect $TV + L1$ in terms of all metrics except Xydeas.

5.C.2. Patient "B"

In the right breast of Patient "B," direct estimation of map using direct $TV + L1$ perform better or at par with indirect estimation using DL in all metrics as shown in Fig. 11(a).

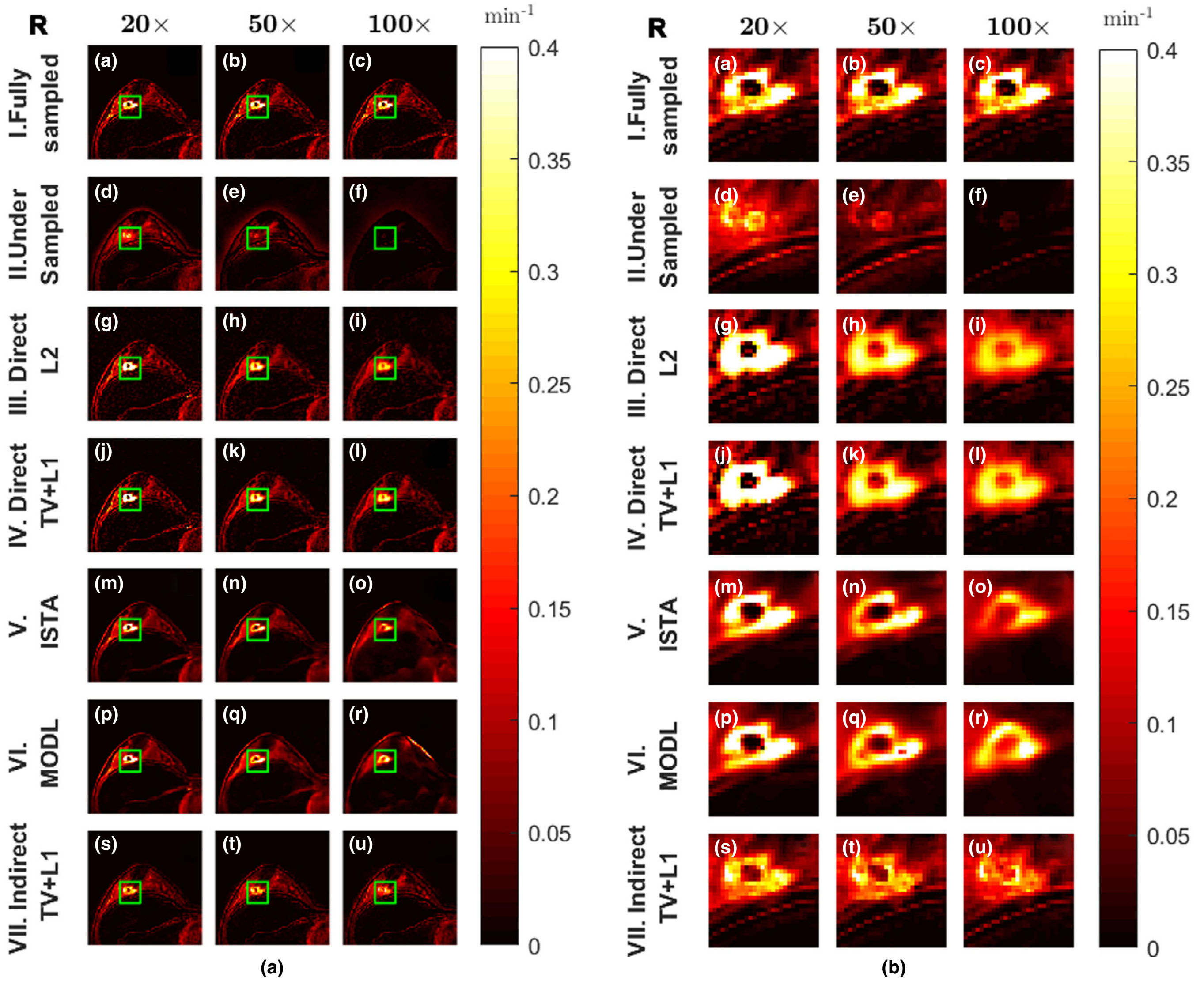

(a)

(b)

FIG. 9. This figure illustrates the reconstructed K_{trans} map for one representative slice of (a) the right breast along with ROI and (b) the zoomed version of ROI (green color bounded box in (a)) of patient "B." It compares the map for different undersampling rates (**R** (column wise)), reconstructed (row wise) from I. Fully sampled data, II. Undersampled data with zero padding, III. $L2$ (no regularization)-based direct reconstruction, IV $TV + L1$ regularized direct reconstruction, V. ISTA-Net^{+}-based indirect reconstruction, VI. MODL-based indirect reconstruction and VII. $TV + L1$-based indirect reconstruction. The wall on which the tumor rests is the boundary of breast implants. In (a) it can be seen that as the **R** increases $L2$-based direct reconstruction becomes noisy. DL- based methods gives blurred results. $TV + L1$-based reconstruction gives less noisy results and causes less blurring. In (b) it can be seen that $TV + L1$ and $L2$ preserves the interior and exterior boundary of the tumor for 20× **R** but the boundary get diffused for higher **R**. The DL-based methods miss correct estimation of boundary for 100× **R**. Indirect $TV + L1$ estimates a hypo-permeable region in tumor and for 100× the internal and external boundaries of tumor are no longer distinct. [Color figure can be viewed at wileyonlinelibrary.com]

Whereas, DL performs better than indirect $TV + L1$ in terms of PSNR and nRMSE and the results are comparable in terms of SSIM. Indirect $TV + L1$ performs better than direct method in terms of Xydeas metric. $L2$ performance is comparable to DL-based methods in terms of PSNR, nRMSE and SSIM and outperforms the latter in Xydeas metric. Same can be inferred from Fig. 9(a) as the map estimated using DL-based methods shows loss of texture and edges including the implant wall. Specular noise is visible in map estimated using $L2$ which is better handled by direct $TV + L1$. In ROI, direct $TV + L1$ and $L2$ perform better than DL for all metrics while the former outperforms the latter as seen in Fig. 11(b). In ROI, the map estimated using DL shows boundary of tumor which does not match the true boundary as seen in Fig. 9(b). In ROI, DL performs better than indirect $TV + L1$ in all metrics except Xydeas. Direct $TV + L1$ performs better than indirect method in all metrics. The boundary of tumor in map estimated using $L2$ and direct $TV + L1$ matches that of fully sampled better, however both suffers from diffusion effect at boundaries because of which the map value at outer boundary were underestimated and at inner boundary (consisting of dead tissue) is overestimated. Direct $TV + L1$ also suffers from staircase effect near boundaries, but is less pronounced than in DL-based reconstruction.

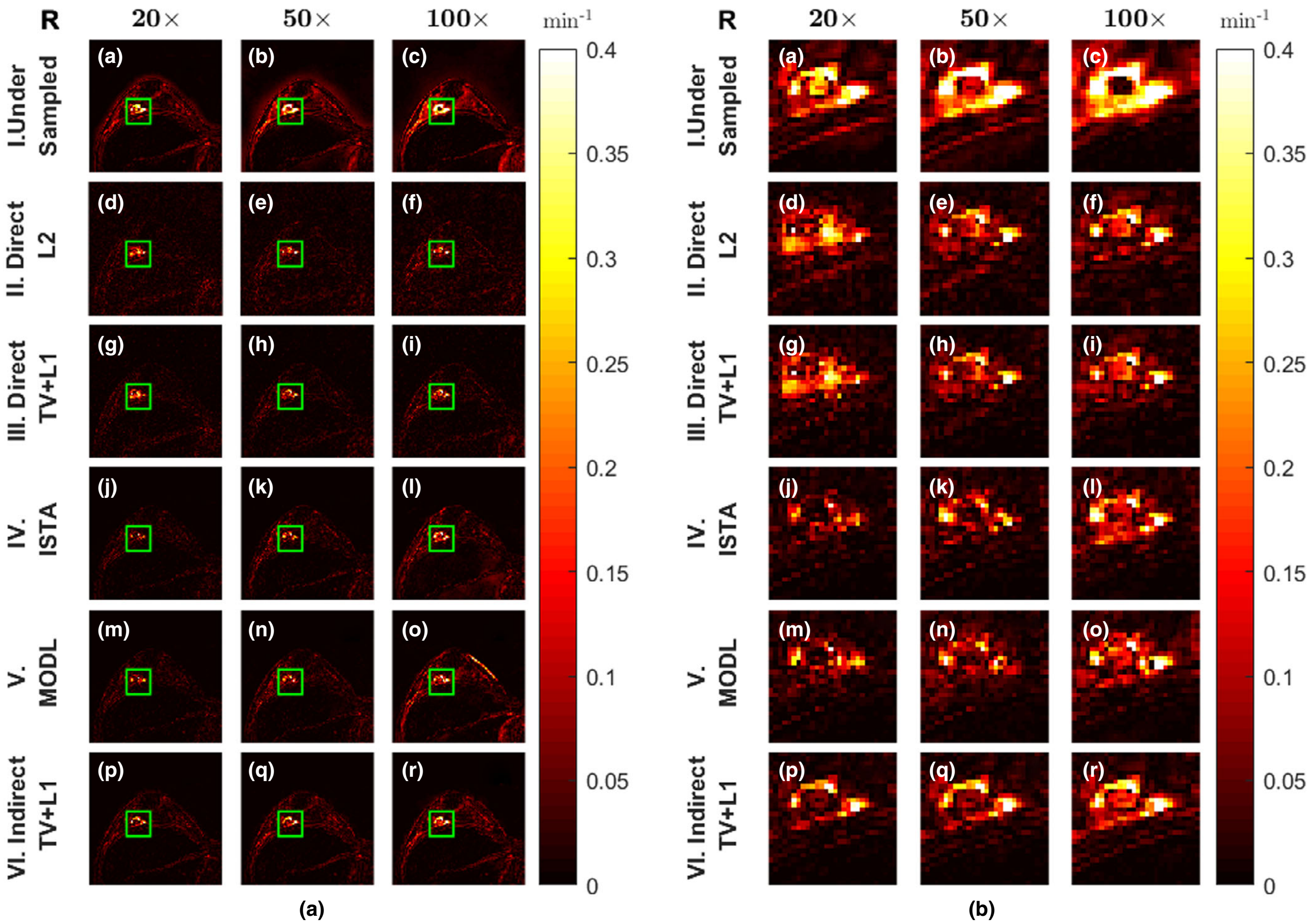

FIG. 10. This figure illustrates the difference between reconstructed K_{trans} map and ground truth for one representative slice of (a) the right breast along with ROI and (b) the zoomed version of ROI (green color bounded box in (a)) of patient "B." It compares the map for different undersampling rates (**R** (column wise)), reconstructed (row wise) from I. Undersampled data with zero padding, II. $L2$ (no regularization)-based direct reconstruction, III $TV + L1$ regularized direct reconstruction, IV. ISTA-Net$^+$-based indirect reconstruction, V. MODL-based indirect reconstruction and VI. $TV + L1$-based indirect reconstruction. The wall on which the tumor rests is the boundary of breast implants. In (a) it can be seen that as the **R** increases indirect methods show higher error in estimating perfusion in fibrous tissues around tumor. In (b) it can be seen that for **R** = 20× DL-based techniques show less error in tumor region. However, for **R** = 100× direct $TV + L1$ shows less error than other techniques. In all cases it can be seen that indirect $TV + L1$ has large errors at both internal and external boundaries. [Color figure can be viewed at wileyonlinelibrary.com]

5.C.3. Average results

Even though the reconstruction of K_{trans} map for only two patients presented in here, the results from other test cases (five patients, 220 slices excluding time dimension) were similar and same trends were observed as in the Patient-"A" and "B." To quantitatively evaluate the performance across all test cases (five patients, 220 slices), the averaged results in terms of figures of merit have been presented in Fig. 12. It is evident that $L2$ and direct $TV + L1$ perform better than the deep learning-based methods (ISTA and MODL) in all metrics for both, whole breast regions and the ROI. This figure also shows that as **R** increases, the average performance of both direct and indirect reconstruction methods fall however the performance of indirect methods of reconstruction using DL-based methods is sub-par compared to direct methods and, therefore, the gap between the performance of direct reconstruction methods that utilize sparse recovery techniques and indirect methods using DL keeps increasing. Table IV shows that the direct $TV + L1$ performs better in five cases in terms of PSNR and in all five cases in terms of SSIM. In terms of ROI results (Table V), the direct $TV + L1$ performs better in four cases and significantly better in three in terms of PSNR and in terms of SSIM the former performs significantly better in all five cases.

5.D. Uniform spiral undersampling mask

We conducted an experiment by changing the undersampling mask from the Radial Golden Angle (RGA) one (which was utilized for the results presented till now) to uniform density spiral. Direct reconstruction and DL-based (trained on RGA pattern) reconstruction techniques were tested for their performance on uniform density spiral undersampling mask. The two patterns are shown in Fig. 13. Uniform density spiral mask was tested on same slices of patient "A" and "B" as shown in Figs. 6 and 9, respectively. The results for patient "A" for spiral

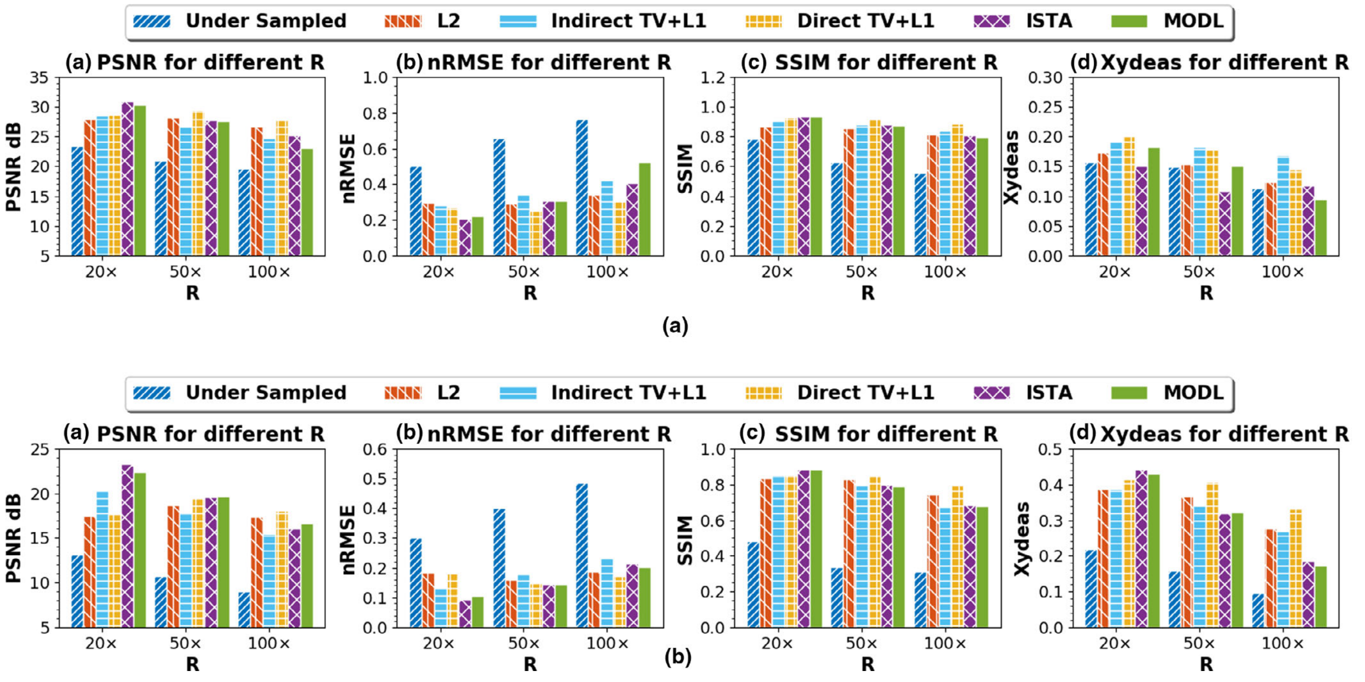

FIG. 11. Comparison of figures of merit, as discussed in Section 4.C., using different reconstruction methods presented in Section 3 for patient “B” (representative images are given in Fig. 9), in (a) right breast and (b) in ROI. Same trends as observed in patient “A” (Fig. 8) are valid here. [Color figure can be viewed at wileyonlinelibrary.com]

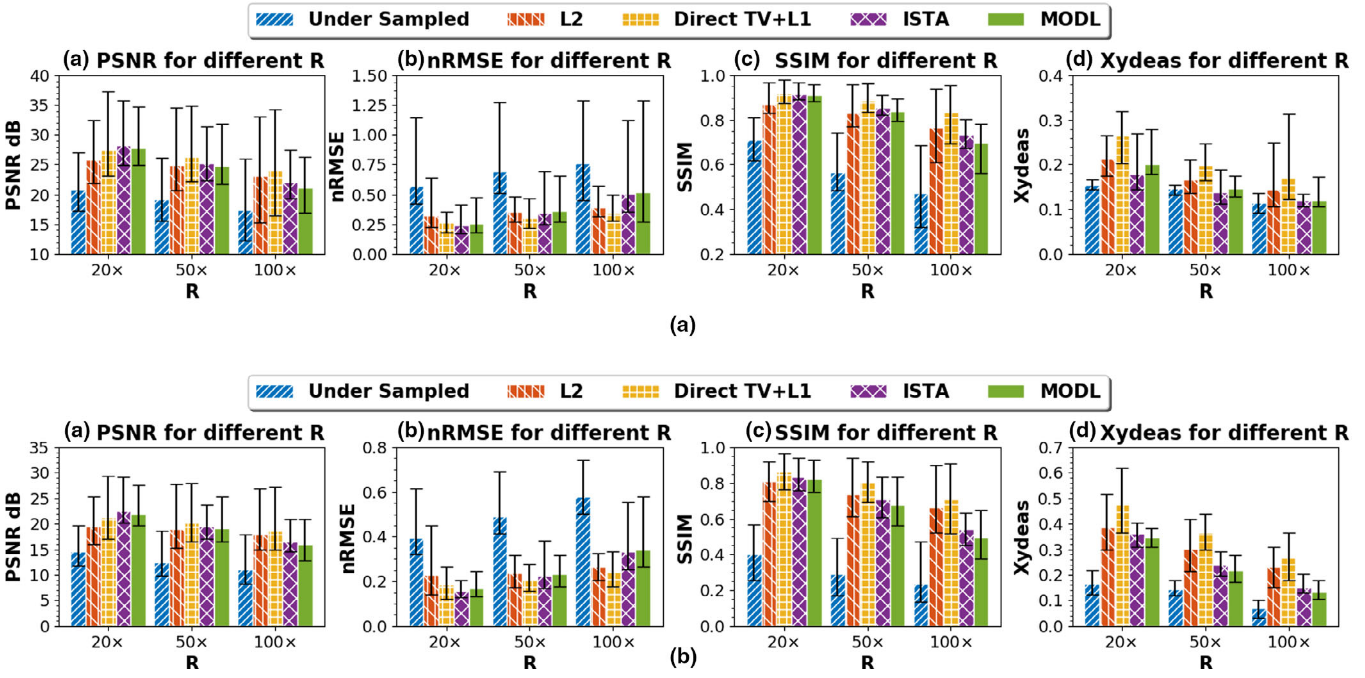

FIG. 12. Comparison between K_{trans} map generated from fully sampled data and from undersampled data using reconstruction techniques mentioned in text for all test cases (five patients data) considered in this work. The results show the average and extremum value of metrics in (a) the breast containing the pathology and (b) the ROI of tumor. In (a) for R being 20×, performance of DL-based methods (ISTA-Net$^+$ and MODL) is better or comparable to direct $TV + L1$. However, in Xydeas metric, performance of direct $TV + L1$ is superior. For 50×, direct $TV + L1$ performs better in all figures of merit while $L2$ and DL provides comparable results. For 100× both $L2$ and direct $TV + L1$ performs better than DL with $TV + L1$ performing the best in all metrics. In (b) for $\mathbf{R}$ being 20×, DL performs better in terms of PSNR and nRMSE, whereas direct $TV + L1$ on average performs marginally better in terms of SSIM and gives considerable improvement in terms of Xydeas metric. For 50×, direct $TV + L1$ performs better on average compared to other methods for all metrics while $L2$ performs comparable to DL in terms of PSNR & nRMSE and better than DL in terms of other metrics. For 100× both $L2$ and direct $TV + L1$ outperform the DL- based method, with direct $TV + L1$ being best in the lot. [Color figure can be viewed at wileyonlinelibrary.com]

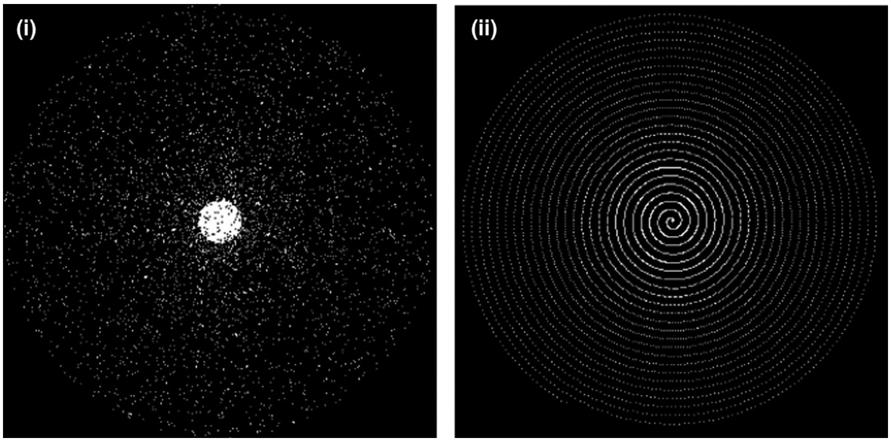

FIG. 13. The undersampling masks for **R** = 20× using (a) Radial Golden angle (RGA) pattern, and (b) Uniform density spiral pattern.

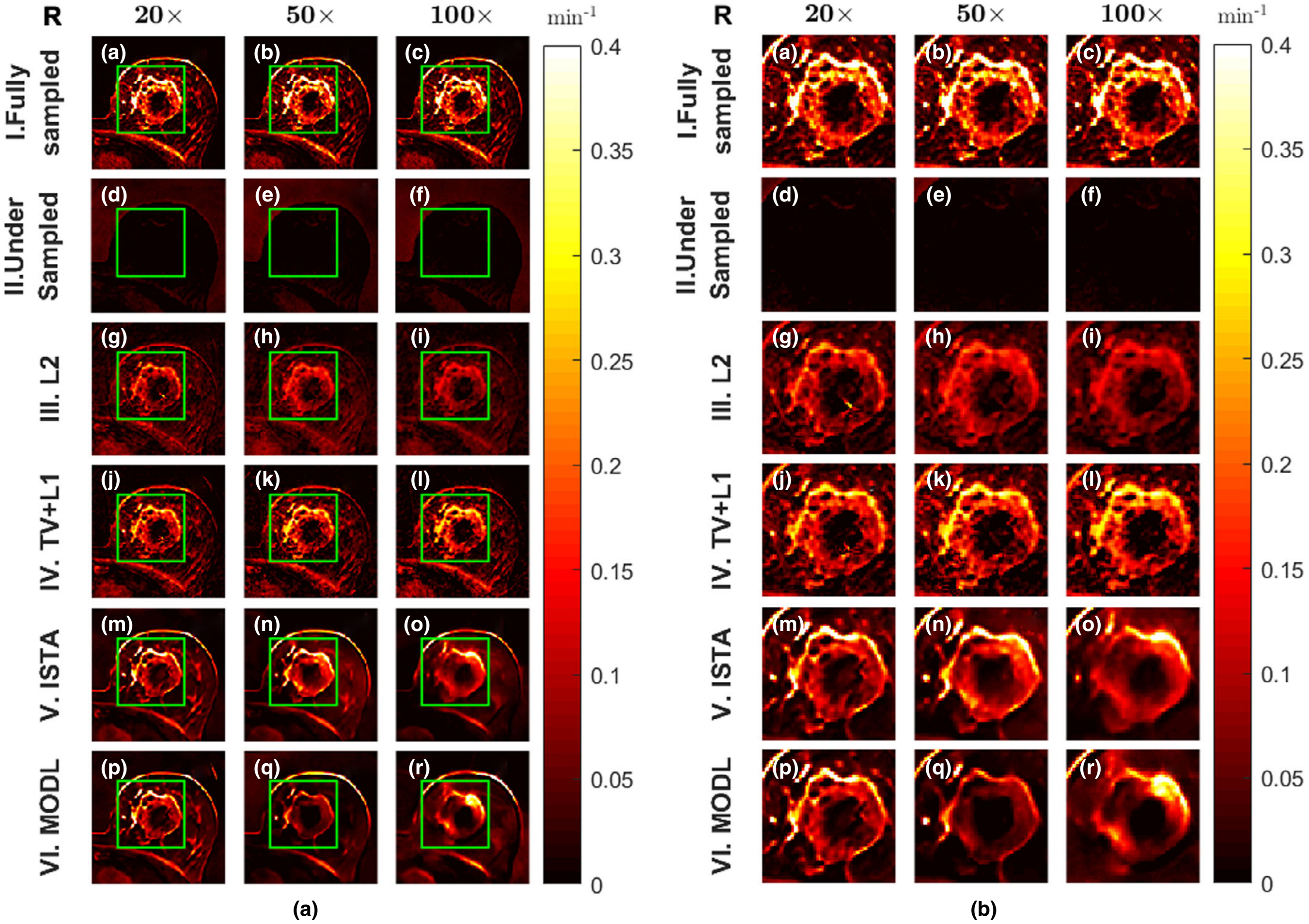

FIG. 14. Same effort as Fig. 6 for the case of uniform density spiral undersampling mask utilizing patient “A” data. Comparing it with Fig. 6 it can be seen that direct iterative methods give better results for a different undersampling pattern than DL-based methods. The quantitative comparison in terms of PSNR and SSIM has been provided in Fig. 15. [Color figure can be viewed at wileyonlinelibrary.com]

undersampling is shown in Fig. 14 and for patient “B” is shown in Fig. 16. In Fig. 15 we compare the performance of $L2$, direct $TV + L1$ and DL-based indirect reconstruction technique for PSNR and SSIM metrics in both whole breast and ROI region for the two undersampling patterns for a single slice of patient “A.” Similarly, in Fig. 17 comparison between $L2$, direct $TV + L1$ and DL-based indirect reconstruction technique for PSNR and SSIM metrics in both whole breast and ROI region for the two undersampling patterns for a single slice of patient “B” is given.

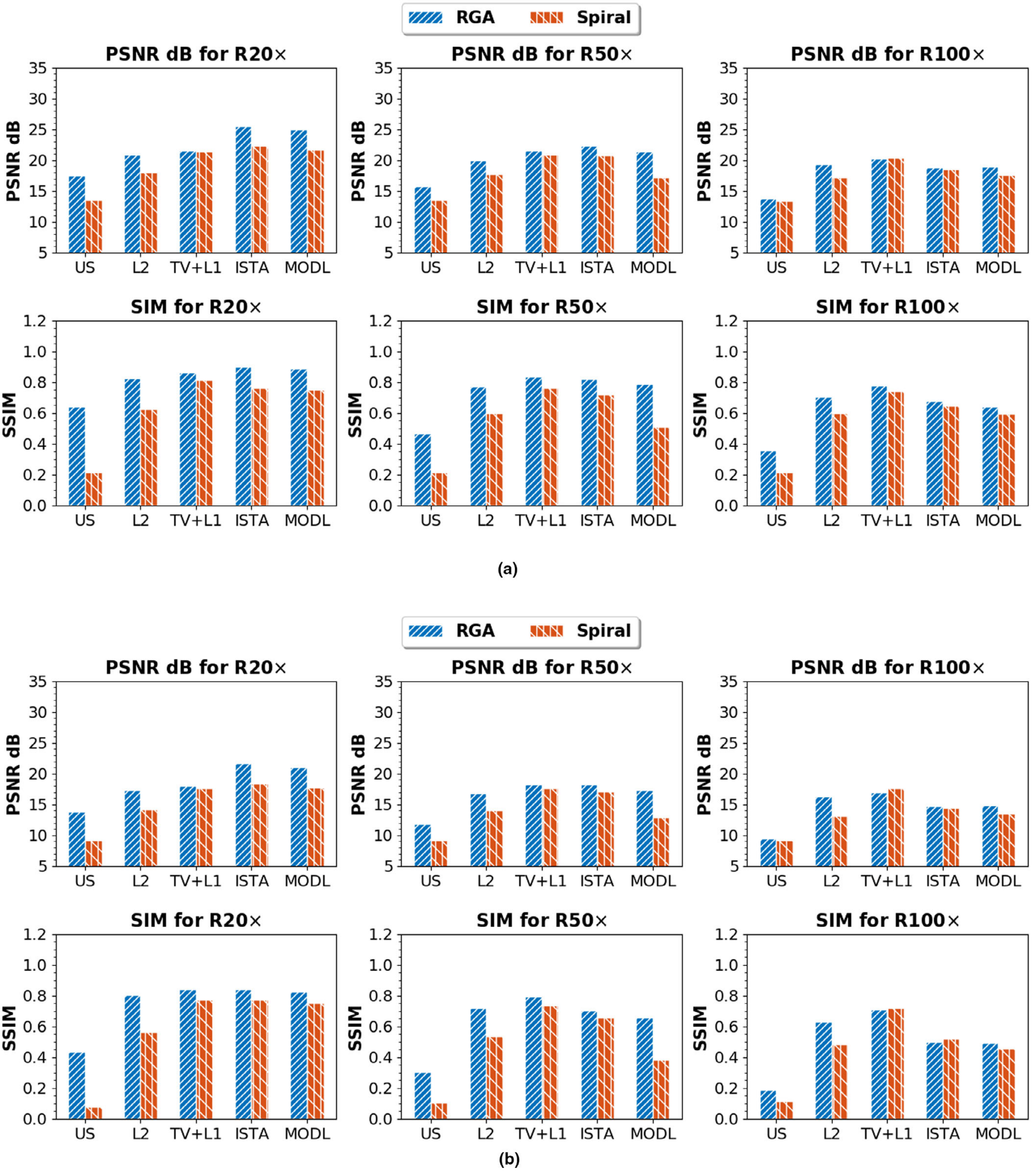

Fig. 15. Comparison of PSNR and SSIM for Radial golden angle and uniform density spiral undersampling masks, using $L2$, direct $TV + L1$ and DL-based reconstruction methods presented in Section 3 for patient “A” (representative images are given in Figs. 6 and 14, respectively), in (a) left breast and (b) in ROI. In (a) for all $\mathbf{R}$, direct $TV + L1$ gives comparable results for both radial golden angle undersampling and spiral undersampling. The performance of DL (trained on radial golden angle mask) drops when tested on spiral masks for both SSIM and PSNR. In (b), the similar trend in performance of direct $TV + L1$ and DL methods for the two undersampling patterns can be observed. [Color figure can be viewed at wileyonlinelibrary.com]

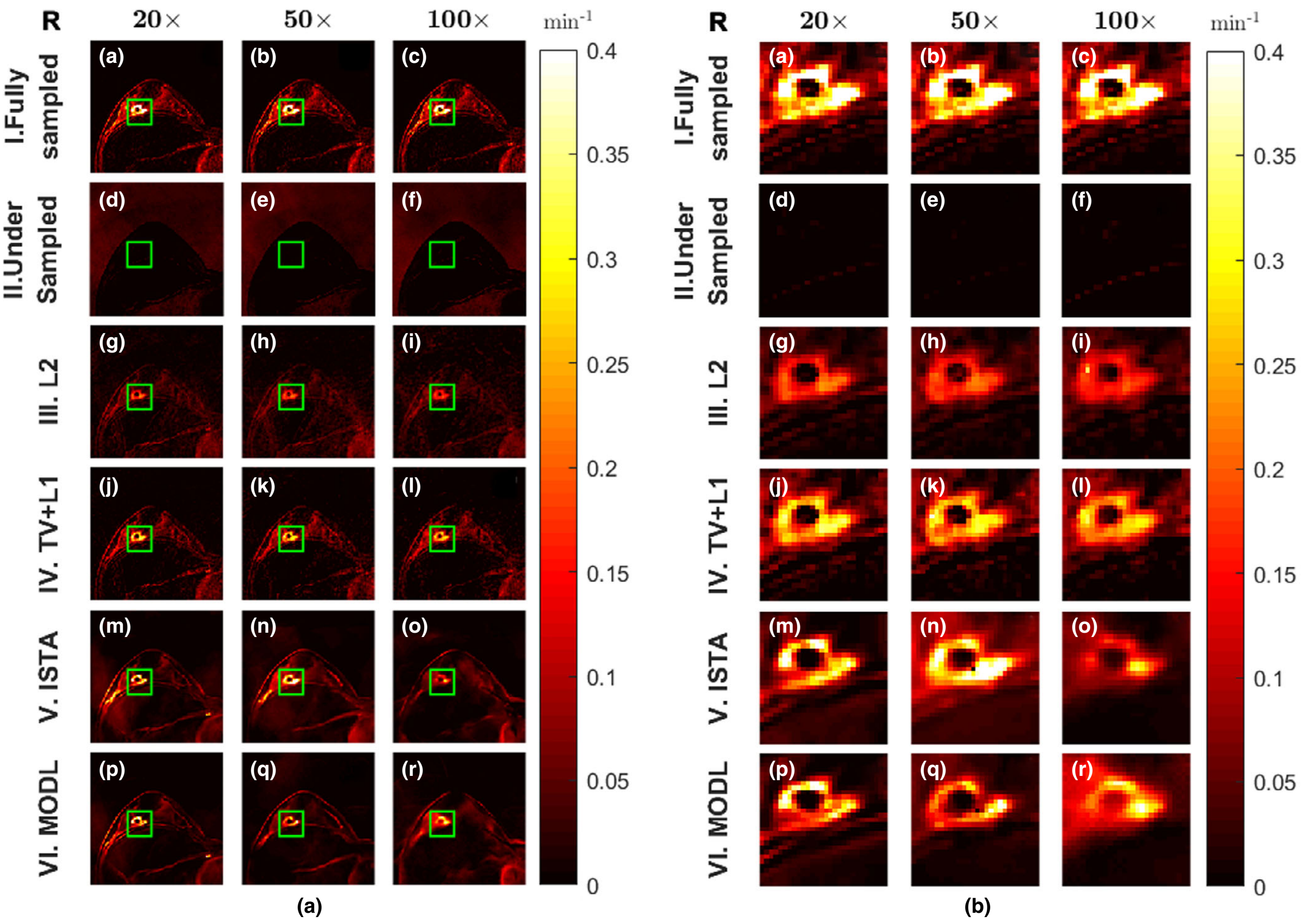

FIG. 16. Same effort as Fig. 9 for the case of uniform density spiral undersampling mask utilizing patient "B" data. Comparing it with Fig. 9 it can be seen that direct iterative methods give better results for a different undersampling pattern than DL-based methods. The quantitative comparison in terms of PSNR and SSIM has been provided in Fig. 17. [Color figure can be viewed at wileyonlinelibrary.com]

5.D.1. Patient "A"

From Fig. 14(a), it is obvious that for all **R** there is no visible information present in the tumor region in undersample estimate. As **R** increases the DL reconstructed technique shows smoothening in ROI. For 100× the DL reconstruction shows diffused tumor boundaries. $L2$ reconstruction preserves the edges and texture but is hypo-permeable. Direct $TV + L1$ shows better overall reconstruction compared to other methods. From Fig. 14(b), it can be observed that all reconstruction methods show less perfusion in ROI for uniform density spiral undersampling, however this effect is minimum in direct $TV + L1$. It can also be seen that the fibrous tissues adjacent to the ROI are better reconstructed by direct TV_L1 method than other techniques. In Fig. 15(a), it can be seen that for all **R**, direct $TV + L1$ perform similar for both sampling patterns in whole breast. However, DL trained and tested on RGA sampling mask outperforms DL tested on spiral mask in terms of both PSNR and SSIM. Direct $TV + L1$ performs better in terms of SSIM for RGA. In ROI as shown in Fig. 15(b), one can observe the same trend for PSNR, however uniform density spiral undersampling provides marginally better SSIM for 100× undersampling in case of DL.

5.D.2. Patient "'B"

From Fig. 16(a), the same trens as observed in patient "A" case. All reconstructed maps were hypo-permeable compared to maps generated from fully sampled data. Same can be inferred from Fig. 16(b), however this effect is minimal for direct $TV + L1$. Moreover, as **R** increases, direct iterative techniques conserve the shape of the tumor, unlike DL-based techniques. In Fig. 17(a), it can be observed that for all **R**, both direct $TV + L1$ and DL perform better for RGA pattern. However the difference in performance of DL for the two patterns is more. The same is true for SSIM as well. In ROI, as shown in Fig. 17(b), in terms of PSNR the performance of DL with spiral pattern is considerably lower compared to RGA pattern. However, direct $TV + L1$ performs similar for both patterns. In terms of SSIM for ROI, we notice the same trend as for PSNR.

6. DISCUSSION & LIMITATIONS

6.A. Discussion

As mentioned in previous section, as **R** increases the information present in K_{trans} map estimated with zero padding decreases. This is due to loss of high frequency information

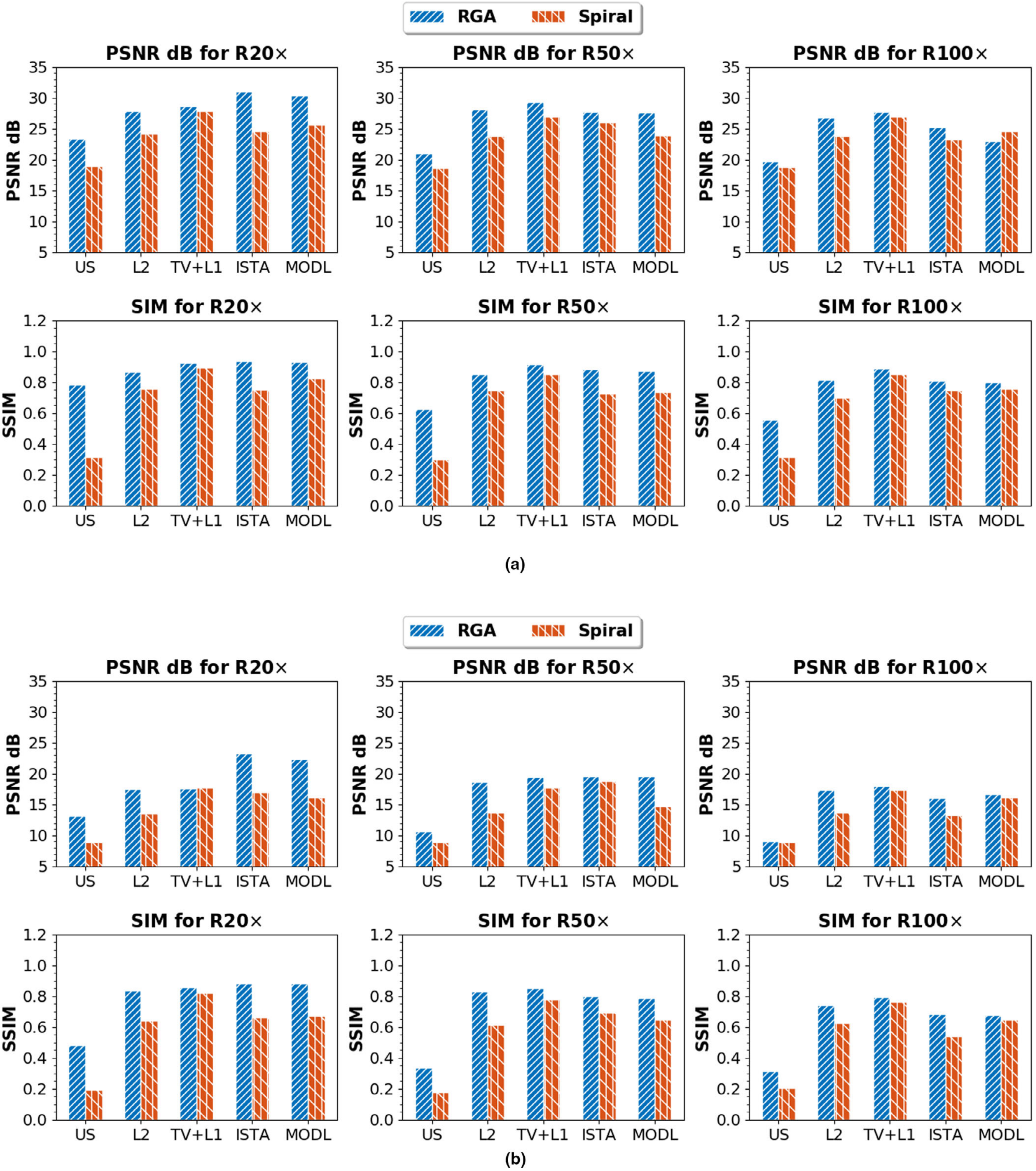

FIG. 17. Comparison of PSNR and SSIM for Radial golden angle and uniform density spiral undersampling masks, using $L2$, direct $TV + L1$ and DL reconstruction methods presented in Section 3 for patient “B” (representative images are given in Fig. 9 and 16, respectively), in (a) right breast and (b) in ROI. In (a) for all **R**, direct $TV + L1$ gives comparable results for both radial golden angle undersampling and spiral undersampling. The trends are similar to those observed in Fig. 15. [Color figure can be viewed at wileyonlinelibrary.com]

in k-t space, which causes loss of data in image space and these errors get propagated to the K_{trans} map. However using the methods mentioned in previous sections, we were able to estimate the K_{trans} map for $\mathbf{R} \in \{20\times,50\times,100\times\}$ more accurately. On basis of Fig. 12, for 20×, the DL-based indirect method of map estimation performs better than or at par with other methods in terms of PSNR, nRMSE, and SSIM. However, for Xydeas metric which compares the edge information in the original map and reconstructed map, direct reconstruction using iterative schemes ($L2$ and $TV + L1$) performs better. The possible reason for this is that deep learning-based methods generalize the breast tissue characteristics and as breast tissue heterogeneity is larger among patient population[26] (density of breast is widely varying among population), the generalization misses out high-frequency structures (edges) in reconstructed images. This leads to loss of edge information as seen in Fig. 6(b) for all values of **R**. For higher **R** values, the performance of direct $TV + L1$ either matches or surpasses that of DL-based methods. There are mainly two reasons for it, first, being the problem of generalization which becomes more difficult as **R** increases and this leads to inaccurate reconstruction of tissue texture. Second, being the indirect method of estimation itself. Because DL-based methods are indirect methods of estimation of K_{trans} maps, the error gets accumulated in each step, from going to image domain $s(\mathbf{r},t)$ to concentration values $CA(\mathbf{r}, t)$ and further down to $K_{trans}(\mathbf{r})$. In the case of direct reconstruction of map, the value of $K_{trans}(\mathbf{r})$ is itself optimized such that the error is minimized, as shown in Eqs. (9) and (10). These two reasons explains the degradation of performance of DL-based indirect methods of reconstruction. Another disadvantage of indirect DL-based method is that the performance deteriorates when tested on an undersampling pattern different from the pattern used for training as seen in Figs. 15 and 17. In these cases, the performance of direct $TV + L1$ is more consistent. Also, from 8 and Fig. 11, it can be inferred that the indirect DL-based estimation is more accurate than indirect $TV + L1$-based estimation for all **R** in terms of SSIM, PSNR, and nRMSE. However, the latter performs better in terms of Xydeas metric as the generalization in DL causes loss of texture in case of inhomogeneous data like breast tissues.

6.B. Limitations

There are some inherent limitations in the methods we utilized for reconstructing the K_{trans} map from the undersampled k-t space data. The Patlak model was chosen for this study based on error as shown in Eq. (1). Although this model gives the advantage of linear approximation and a convex solution, it may not fit all datasets accurately. Taking higher order models will have a shortcoming of higher error between forward and inverse model and will make Eq. (2) non-linear and non-convex. Methods like l-BFGS[33] will be needed to solve this step which will make the computation more expensive.

The second limitation of our experiments is the choice of prior in K_{trans} regularization. As shown above in section 5, the $\|\cdot\|_{TV}$ gives staircase effect, a solution to this is to use total generalized variation (TGV)[48] which is shown to be free from this artifact. This will be taken up as future work to further improve the framework.

The third limitation of this study is the choice of dataset. The organ of interest in this work was breast and breast tissue density is known to be inhomogeneous[28] across the population and with age compared to other tissues. This is caused by varying distribution of fibrous, glandular and fatty tissue and leads to variation in tissue texture among the population. This makes generalization using any DL technique difficult for reconstruction. Therefore, the trend of performance for the breast imaging case might not be same for other DCE-MR imaging cases.

Other limitation is that deep learning-based methods utilized here were generic, mostly to solve inverse problems in terms of MR image reconstruction, and only employed for indirect estimation of K_{trans}. These DL-based methods were known to be solving generic inverse problems and is agnostic to the problem at hand. So these methods may not provide optimal performance especially for increased under sampling rates compared to sparse recovery methods. However, this study also shows that deep learning-based methods may not be suitable for all cases and can only provide optimal performance where generalization is not challenging. The information retrieval of DL models is dependent on available data (they are generally data hungry), requiring large scale training data, which is not always possible especially medical imaging/physics areas. In these cases, it has been shown through this work that traditional sparse recovery methods hold value.

7. CONCLUSIONS

In this work, direct and indirect estimation of TK parameters using iterative schemes were compared with indirect estimation of TK parameters using DL methods, from undersampled k-t space data. The undersampling rates that were used are 20×, 50× and 100×. We compared the performance of these methods on DCE-MRI data of breast tissues of five patients by retrospectively undersampling the data. The K_{trans} map generated from fully sampled data were considered as ground truth and we compared the performance of direct and indirect estimation methods using PSNR, n-RMSE, SSIM and Xydeas metric. On the basis of these experiments, we observe that for breast DCE-MRI data of inhomogeneous population, direct reconstruction of K_{trans} using direct $TV + L1TV + L1$ regularization performs better than indirect estimation methods (iterative as well as DL methods) for higher undersampling rates (50× and 100×). We have also provided detailed explanation of our observations and have highlighted the limitations of both approaches. We have also discussed the way forward to address some of these limitations and plan to pursue them as part of future work. The developed code was made available as https://github.com/Medical-Imaging-Group/DCE-MRI-Compare open-source for enthusiastic users as well as to enable further investigations.

ACKNOWLEDGMENTS

The authors are thankful to Dr. Wei Huang of Oregon Health & Science University and The Cancer Imaging Archive for providing the required breast DCE-MR imaging data as open-source for carrying out this work. This work was funded by the Science & Engineering Research Board (SERB) core research grant (No. CRG/2018/000672).

CONFLICT OF INTEREST

There are no conflict of interest declared by Authors.

[a]Author to whom correspondence should be addressed. Electronic mail: yalavarthy@iisc.ac.in.

REFERENCES

1. Gribbestad IS, Gjesdal KI, Nilsen G, Lundgren S, Hjelstuen MHB, Jackson A. An introduction to dynamic contrast-enhanced MRI in oncology. In *Dynamic contrast-enhanced magnetic resonance imaging in oncology*. Springer; 2005:1–22.
2. Yan Y, Sun X, Shen B. Contrast agents in dynamic contrast-enhanced magnetic resonance imaging. *Oncotarget*. 2017;8:43491.
3. Nagel E, Klein C, Paetsch I, et al. Magnetic resonance perfusion measurements for the noninvasive detection of coronary artery disease. *Circulation*. 2003;108:432–437.
4. Parker GJ, Suckling J, Tanner SF, Padhani AR, Husband JE, Leach MO. MRIW: parametric analysis software for contrast-enhanced dynamic MR imaging in cancer. *Radiographics*. 1998;18:497–506.
5. Hylton NM, Blume JD, Bernreuter WK, et al. Locally advanced breast cancer: MR imaging for prediction of response to neoadjuvant chemotherapy|results from ACRIN 6657/I-SPY TRIAL. *Radiology*. 2012;263:663–672.
6. Paldino MJ, Barboriak DP. Fundamentals of quantitative dynamic contrast-enhanced MR imaging. *Magnetic Reson Imaging Clin North Am*. 2009;17:277–289.
7. Tofts PS, Kermode AG. Measurement of the blood-brain barrier permeability and leakage space using dynamic MR imaging. 1. Fundamental concepts. *Magn Reson Med*. 1991;17:357–367.
8. Larsson HBW, Stubgaard M, Frederiksen JL, Jensen M, Henriksen O, Paulson OB. Quantitation of blood-brain barrier defect by magnetic resonance imaging and gadolinium-DTPA in patients with multiple sclerosis and brain tumors. *Magn Reson Med*. 1990;16:117–131.
9. Patlak CS, Blasberg RG, Fenstermacher JD. Graphical evaluation of blood-to-brain transfer constants from multiple-time uptake data. *J Cerebr Blood Flow Metab*. 1983;3:1–7. PMID: 6822610.
10. Brix G, Semmler W, Port R, Schad LR, Layer G, Lorenz WJ. Pharmacokinetic parameters in CNS Gd-DTPA enhanced MR imaging. *J Comput Assist Tomogr*. 1991;15:621–628.
11. Tofts PS, Brix G, Buckley DL, et al. Estimating kinetic parameters from dynamic contrast-enhanced T1-weighted MRI of a diffusable tracer: standardized quantities and symbols. *J Magn Reson Imaging*. 1999;10: 223–232.
12. Brix G, Kiessling F, Lucht R, et al. Microcirculation and microvasculature in breast tumors: pharmacokinetic analysis of dynamic MR image series. *Magn Reson Med*. 2004;52:420–429.
13. Sangren WC, Sheppard CW. A mathematical derivation of the exchange of a labeled substance between a liquid owing in a vessel and an external compartment. *Bullet Math Biophys*. 1953;15:387–394.
14. Johnson JA, Wilson TA. A model for capillary exchange. *Am J Physiol-Leg Cont*. 1966;210:1299–1303.
15. Jaspan ON, Fleysher R, Lipton ML. Compressed sensing MRI: a review of the clinical literature. *Br J Radiol*. 2015;88:20150487.
16. Smith DS, Welch EB, Li X, et al. Quantitative effects of using compressed sensing in dynamic contrast enhanced MR. *Phys Med Biol*. 2011;56:4933.
17. Feng L, Grimm R, Block KT, et al. Golden-angle radial sparse parallel MRI: combination of compressed sensing, parallel imaging, and golden-angle radial sampling for fast and flexible dynamic volumetric MRI. *Magn Reson Med*. 2014;72:707–717.
18. Rosenkrantz AB, Geppert C, Grimm R, et al. Dynamic contrast enhanced MRI of the prostate with high spatiotemporal resolution using compressed sensing, parallel imaging, and continuous golden-angle radial sampling: preliminary experience. *J Magn Reson Imaging*. 2015;41:1365–1373.
19. Guo Y, Lingala SG, Zhu Y, Lebel RM, Nayak KS. Direct estimation of tracer-kinetic parameter maps from highly undersampled brain dynamic contrast enhanced MRI. *Magn Reson Med*. 2017;78:1566–1578.
20. Guo Y, Lingala SG, Bliesener Y, Lebel RM, Zhu Y, Nayak KS. Joint arterial input function and tracer kinetic parameter estimation from undersampled dynamic contrast-enhanced MRI using a model consistency constraint. *Magn Reson Med*. 2018;79:2804–2815.
21. Dikaios N, Arridge S, Hamy V, Punwani S, Atkinson D. Direct parametric reconstruction from undersampled (k, t)-space data in dynamic contrast enhanced MRI. *Med Image Anal*. 2014;18:989–1001.
22. Bliesener Y, Acharya J, Nayak KS. Efficient DCE-MRI parameter and uncertainty estimation using a neural network. *IEEE Trans Med Imaging*. 2019;39:1712–1723.
23. Ulas C, Das D, Thrippleton MJ, et al. Convolutional neural networks for direct inference of pharmacokinetic parameters: application to stroke dynamic contrast-enhanced MRI. *Front Neurol*. 2018;9:1147.
24. Ulas C, Tetteh G, Thrippleton MJ, et al. Direct Estimation of Pharmacokinetic Parameters from DCE-MRI using Deep CNN with Forward Physical Model Loss. In *International Conference on Medical Image Computing and Computer-Assisted Intervention*. Springer; 2018: 39–47.
25. Kettelkamp J, Lingala SG. Arterial input function and tracer kinetic model-driven network for rapid inference of kinetic maps in Dynamic Contrast-Enhanced MRI (AIF-TK-net). In: *IEEE 17th International Symposium on Biomedical Imaging (ISBI)*. IEEE; 2020:1450–1453.
26. Zhang J, Ghanem B. ISTA-Net: Interpretable optimization-inspired deep network for image compressive sensing. In *Proceedings of the IEEE conference on computer vision and pattern recognition* 2018:1828–1837.
27. Aggarwal HK, Mani MP, Jacob M. MoDL: Model-based deep learning architecture for inverse problems. *IEEE Trans Med Imaging*. 2018;38: 394–405.
28. Valentin J. Basic anatomical and physiological data for use in radiological protection: reference values: ICRP Publication 89: approved by the Commission in September 2001. *Ann ICRP*. 2002;32:1–277.
29. Rockafellar RT. Monotone operators and the proximal point algorithm. *SIAM J Control Optim*. 1976;14:877–898.
30. Boyd S, Parikh N, Chu E, Peleato B, Eckstein J. others. Distributed optimization and statistical learning via the alternating direction method of multipliers. *Found Trends® Mach Learn*. 2011;3:1–122.
31. Chan SH, Wang X, Elgendy OA. Plug-and-play ADMMfor image restoration: fixed-point convergence and applications. *IEEE Trans Comput Imaging*. 2016;3:84–98.
32. Tirer T, Giryes R. Image restoration by iterative denoising and backward projections. *IEEE Trans Image Process*. 2018;28:1220–1234.
33. Liu DC, Nocedal J. On the limited memory BFGS method for large scale optimization. *Math Program*. 1989;45:503–528.
34. Lustig M, Donoho D, Pauly JM. Sparse MRI: the application of compressed sensing for rapid MR imaging. *Magnet Reson Med*. 2007;58:1182–1195.
35. Venkatakrishnan SV, Bouman CA, Wohlberg B. Plug-and-play priors for model based reconstruction. In: *IEEE Global Conference on Signal and Information Processing*. IEEE; 2013:945–948.
36. Huang W, Li X, Chen Y, et al. Variations of dynamic contrast-enhanced magnetic resonance imaging in evaluation of breast cancer therapy response: a multicenter data analysis challenge. The Cancer Imaging Archive. http://doi.org/10.7937/K9/TCIA.2014.A2N1IXOX 2014.
37. Clark K, Vendt B, Smith K, et al. The Cancer Imaging Archive (TCIA): maintaining and operating a public information repository. *J Digit Imaging*. 2013;26:1045–1057.
38. Huang W, Li X, Chen Y, et al. Variations of dynamic contrast-enhanced magnetic resonance imaging in evaluation of breast cancer therapy response: a multicenter data analysis challenge. *Transl Oncol*. 2014;7:153–166.
39. Le Y, Kroeker R, Kipfer HD, Lin C. Development and evaluation of TWIST Dixon for dynamic contrast-enhanced (DCE) MRI with improved acquisition efficiency and fat suppression. *J Magn Reson Imaging*. 2012;36:483–491.
40. Li X, Abramson RG, Arlinghaus C, et al. Data From QIN-Breast. The Cancer Imaging Archive http://doi.org/10.7937/K9/TCIA.2016.21JUeb H0 2016.
41. Li X, Abramson RG, Arlinghaus LR, et al. Multiparametric magnetic resonance imaging for predicting pathological response after the first cycle of neoadjuvant chemotherapy in breast cancer. *Invest Radiol*. 2015;50:195–204.

42. Lehman CD, Mahoney M, Newell M, Radiology American College. others. ACR practice parameter for the performance of contrast-enhanced magnetic resonance imaging (MRI) of the breast. https://www.acr.org/-/media/ACR/Files/Practice-Parameters/mr-contrast-breast.pdf 2014.
43. Kingma DP, Ba J. Adam: A method for stochastic optimization. *arXiv preprint arXiv:1412.6980*. 2014.
44. Wang Z, Bovik AC, Sheikh HR, Simoncelli EP. Image quality assessment: from error visibility to structural similarity. *IEEE Trans Image Process*. 2004;13:600–612.
45. Xydeas CS, Petrovic V. Objective image fusion performance measure. *Electron Lett*. 2000;36:308–309.
46. Jung SC, Yeom J, Kim J-H, et al. Glioma: application of histogram analysis of pharmacokinetic parameters from T1-weighted dynamic contrast-enhanced MR imaging to tumor grading. *Am J Neuroradiol*. 2014;35:1103–1110.
47. Šidák Z. Rectangular confidence regions for the means of multivariate normal distributions. *J Am Statist Ass*. 1967;62:626–633.
48. Bredies K, Kunisch K, Pock T. Total generalized variation. *SIAM J Imaging Sci*. 2010;3:492–526.